Research Square

Preprints are preliminary reports that have not undergone peer review.
They should not be considered conclusive, used to inform clinical practice,
or referenced by the media as validated information.

Downsizing a BTK PROTAC yields a G-loop independent molecular glue that blurs the boundary between degrader classes

Jin Wang

wang.j@bcm.edu

Baylor College of Medicine https://orcid.org/0000-0003-3625-7919

Ran Cheng

Baylor College of Medicine

Hanfeng Lin

Baylor College of Medicine https://orcid.org/0000-0002-3172-5616

Lukáš Maršálek

Eyen SE

Deepak Pathak

Rice University

Xin Yu

Baylor College of Medicine

Shrilekha Misra

The Ohio State University Comprehensive Cancer Center

Andrew Mitchell

The Ohio State University Comprehensive Cancer Center

Jennifer Woyach

The Ohio State University https://orcid.org/0000-0002-3403-9144

Yang Gao

Rice University https://orcid.org/0000-0002-4037-0431

Xiaoli Qi

Baylor College of Medicine https://orcid.org/0009-0007-4531-7449

Article

Keywords:

Posted Date: November 6th, 2026

DOI: https://doi.org/10.21203/rs.3.rs-11296825/v1

License: This work is licensed under a Creative Commons Attribution 4.0 International License.
Read Full License

Additional Declarations: Yes there is potential Competing Interest. The authors declare the following competing financial interest(s): J.W. is a co-founder of Chemical Biology Probes, LLC. and serves as a consultant for CoRegen Inc. J.W. and X.Y. are co-founders of Fortitude Biomedicines, Inc. and hold equity interest in this company. R.C., H.L., X.Y., X.Q., and J.W. are the co-inventors on a patent related to this work. J.A.W. consults for AstraZeneca, AbbVie, BeOne, Genentech, Johnson & Johnson, Loxo@Lilly, Merck, and Newave. The remaining authors declare no competing interests.

Downsizing a BTK PROTAC yields a G-loop independent molecular glue that blurs the boundary between degrader classes

Ran Cheng [a,b,¶,*], Hanfeng Lin [a,b,¶], Lukáš Maršálek [c], Deepak Pathak [d], Xin Yu [a,b], Shrilekha Misra [e], Andrew D. Mitchell [e], Jennifer A. Woyach [e], Yang Gao [d], Xiaoli Qi [a,b,*], Jin Wang [a,b,f,*]

[a.] The Verna and Marrs McLean Department of Biochemistry and Molecular Pharmacology, Baylor College of Medicine, Houston, Texas 77030, United States.

[b.] Center for NextGen Therapeutics, Baylor College of Medicine, Houston, Texas 77030, United States.

[c.] Eyen SE, Počernická 272/96, 108 00 Prague 10, Czech Republic.

[d.] Department of BioSciences, Rice University, Houston, TX 77005, United States.

[e.] Division of Hematology, The Ohio State University Comprehensive Cancer Center, Columbus, Ohio, United States.

[f.] Department of Molecular and Cellular Biology, Baylor College of Medicine, Houston, Texas 77030, United States.

[¶] Contributed equally

* Corresponding email: wangj@bcm.edu; xiaoli.qi@bcm.edu; ran.cheng@bcm.edu

Abstract

Targeted protein degradation (TPD) represents a novel and rapidly evolving therapeutic strategy that harnesses the cell's own proteolytic systems to selectively eliminate disease-associated proteins. In this study, we serendipitously discovered and characterized the first Bruton's tyrosine kinase (BTK)-targeting molecular glue, PS-10. PS-10 efficiently degrades BTK with a DC_{50} in the single-digit nanomolar range and a D_{max} exceeding 95%, despite displaying negligible binary binding affinity for the kinase itself. Cryo-EM and computational modeling revealed that PS-10 induces a protein-protein interaction (PPI) interface between CRBN and BTK stabilized by an induced-fit rotation of the BTK N-lobe, with extensive PPIs distinct from previously known CRBN-substrate complexes. Crucially, global proteomics and mutational mapping across other kinases (CSK, AURKA, LIMK1, and TEC) demonstrated that this degradation mechanism extends beyond BTK and relies on a diverse set of PPI residues. These findings underscore a remarkable structural plasticity, indicating that productive E3-neosubstrate PPIs can be dynamically achieved via distinct structural trajectories. Ultimately, this demonstrates that rigid, pre-existing degrons are not mandatory; rather, the existence of even a weak target binder presents a distinct opportunity to exploit plastic PPI interfaces to maximize cooperativity, establishing a novel and generalizable blueprint for rational molecular glue design.

Introduction

The serendipitous discovery of thalidomide's efficacy in treating erythema nodosum leprosum marked the beginning of a new era in targeted protein degradation (TPD). Thalidomide and its derivatives, known as immunomodulatory imide drugs (IMiDs), were found to re-program the ubiquitin-proteasome system (UPS) to selectively degrade neosubstrates such as Ikaros (IKZF1) and Aiolos (IKZF3) through the E3 ubiquitin ligase cereblon (CRBN) [1,2]. Structural biology studies of CRBN-IMiD complexes with various neosubstrates, including casein kinase 1 alpha (CK1α) [3], G1 to S phase transition 1 (GSPT1) [4], and several zinc finger (ZF) proteins [5], unveiled a common structural motif recognized by these complexes. This motif, termed the G-loop, is a three-dimensional protein turn containing an invariant glycine that serves as a shared degron for recruitment by CRBN-IMiD complexes. Historically, the G-loop has emerged as a key determinant of specificity and a primary screening requirement in IMiD-induced protein degradation [6]. Recent reviews have further codified these principles, establishing thermodynamic and structural frameworks for molecular glue discovery. [7,8]

Molecular glues like IMiDs represent a distinct class of protein degraders that offer unique advantages over other degradation strategies such as proteolysis-targeting chimeras (PROTACs) and monovalent degraders [6,9]. While PROTACs and monovalent degraders typically require a high-affinity ligand to bind the target protein, molecular glues primarily bind to the E3 ligase and create a new protein-protein interface that recruits the target protein for degradation [10]. This crucial distinction allows molecular glues to potentially engage proteins that lack well-defined binding pockets or are considered undruggable by conventional approaches.

While early CRBN neosubstrates were strictly defined by the presence of canonical G-loops, a wave of recent structural and proteomic advances has fundamentally redefined the rules of neosubstrate recognition, revealing alternative, G-loop-independent binding modes. This expanding structural paradigm is best exemplified by the recent successful targeting of VAV1, an undruggable guanine nucleotide exchange factor. Monte Rosa Therapeutics discovered highly selective VAV1 molecular glues and subsequently advanced MRT-6160 into clinical trials for autoimmune diseases [11–13]. Concurrently, our group utilized high-throughput proteomics to independently discover novel VAV1 molecular glue hits [14,15]. By integrating AI-driven protein folding predictions with rigorous mutagenesis validation, we successfully elucidated the underlying structural basis for this interaction, revealing a novel, non-canonical RT-loop degron (the RDxS motif) within the VAV1

SH3 domain [14]. Furthermore, recent studies identified G3BP2 as another non-canonical neosubstrate that bypasses the classic G-loop requirement by engaging an unconventional binding site on the CRBN LON domain through molecular surface mimicry of an endogenous protein-protein interaction (PPI) hotspot [16]. The remarkable structural plasticity of CRBN is also highlighted by the discovery of degron-mimicking molecular glues (such as MRT-31619) that drive CRBN homo-dimerization [17]; in this unique mechanism, two glue molecules assemble into a helix-like structure to mimic a neosubstrate G-loop, triggering CRBN's own degradation. Together, these breakthroughs firmly establish that CRBN can recognize a highly diverse landscape of structural motifs beyond the canonical G-loop, opening the door for the rational design of novel molecular glues targeting a much broader range of the proteome. This rapid expansion in both mechanistic understanding and target scope has accelerated clinical translation, with over 65 molecular glue candidates now in development supported by more than 50 biotech and pharmaceutical organizations [18].

BTK provides a clinically validated setting in which to test this expanded molecular-glue logic. BTK couples B-cell receptor signaling to malignant B-cell survival and immune-cell activation, and genetic studies first linked loss-of-function BTK mutations to X-linked agammaglobulinemia [19,20]. Subsequent clinical studies established covalent BTK inhibition as an effective therapeutic strategy in B-cell malignancies [21]. However, acquired resistance driven by BTK and PLCG2 mutations, including C481 substitutions that prevent irreversible inhibitor engagement, remains a major limitation [22]. Noncovalent inhibitors such as pirtobrutinib can address some covalent-inhibitor resistance mechanisms, but additional BTK kinase-domain mutations and convergent resistance patterns continue to emerge [23,24]. This therapeutic pressure has motivated BTK degraders, including clinically advancing heterobifunctional degraders [25–27], because degradation can remove both catalytic and scaffold functions rather than merely inhibit kinase activity. Yet most reported BTK degraders still rely on high-affinity BTK warheads and PROTAC-like bifunctional architectures, leaving open whether BTK can be recruited through a compact, cooperative molecular glue mechanism.

In this study, we present the serendipitous discovery and comprehensive characterization of PS-10, the first molecular glue targeting Bruton's tyrosine kinase (BTK). PS-10 exhibits remarkable potency in degrading BTK, with a DC_{50} of 2 nM and a maximum degradation (D_{max}) of 98% in Ramos cells. Intriguingly, PS-10 achieves this potent degradation despite demonstrating minimal direct binding affinity for BTK. Instead, PS-10 binds strongly to CRBN, facilitating the formation of a stable ternary complex between BTK, PS-10, and CRBN. This complex formation leads to BTK degradation through a molecular glue mechanism.

Our structural investigations reveal that BTK and CRBN engage in extensive protein-protein interactions within the ternary complex, presenting a binding mode distinct from previously characterized CRBN-neosubstrate structures. Significantly, BTK emerges as another novel G-loop independent neosubstrate, broadening the spectrum of proteins targetable by molecular glues. We further demonstrate that PS-10's molecular glue mechanism extends beyond BTK, effectively degrading other kinases such as CSK, AURKA, LIMK1, and TEC, underscoring the broad applicability of this G-loop independent binding mode in targeted protein degradation. These findings not only advance our understanding of molecular glue degraders but also expand the toolkit for targeting proteins previously considered undruggable. The unique binding and degradation mechanism of PS-10 opens new avenues for the rational design of molecular glues, potentially leading to the development of kinase-selective molecular glues with diverse therapeutic applications.

Results

Discovery of a unique and potent BTK degrader

During our initial efforts to develop BTK PROTACs, we discovered that an ibrutinib-based reversible covalent PROTAC RC-1 could overcome the permeability issue of these large PROTAC molecules and achieve intracellular accumulation as high as BTK inhibitors and CRBN ligands [28]. We subsequently attempted to apply the same reversible covalent chemistry to another BTK inhibitor, poseltinib [29], to develop BTK PROTAC PS-RC-1 (**Figure 1A**). But to our surprise, PS-RC-1 is unable to degrade BTK in cells and exhibits weak binding affinity towards BTK (**Figure S1**). Postulating that the *t*-butyl group in PS-RC-1 may render steric hindrance to prevent its binding to BTK, we performed molecular surgeries to reduce the size of PS-RC-1 and reported PS-2 as a potent BTK degrader [30] (**Figure 1A**). PS-2 was designed to restore BTK engagement by relieving this steric clash, and it degraded BTK potently. Whether that activity arises from conventional bivalent target engagement, however, was not established, especially since PS-2 is much smaller than a typical BTK PROTAC and retains only a short linker. Defining the mechanism underlying this activity is the subject of the present work. We first performed medicinal chemistry optimization of PS-2, which leads to a more potent analog PS-10 (**Figure 1A**). PS-2 and PS-10 degrade BTK in Ramos and Mino cells with DC_{50} in the single-digit nM range as early as 4-8 h after treatment (**Figure 1B, D, E, Figure S2**) and we confirmed the degradation mechanism is dependent on CRBN and is through the ubiquitin-proteasome pathway since degradation was abolished with treatment of methylated glutarimide negative control (PS-10-Me, **Figure 1A**),

or PS-10 co-treated with CRBN covalent binder EM12-SO_2Im [31], E1 inhibitor TAK243, NEDDylation inhibitor MLN4924, or proteasome inhibitor carfilzomib (**Figure 1C**).

What sets PS-2 and PS-10 apart from other BTK PROTACs is their minimal affinity with BTK. In a time-resolved fluorescence resonance energy transfer (TR-FRET) based BTK binding assay (**Figure 2A**), PS-2 and PS-10 have no appreciable competition against the BTK tracer even at 10 μM (**Figure 2B**), underscoring their lack of direct binding affinities. While in the presence of CRBN/DDB1 complex, the IC_{50} values of PS-2 and PS-10 decrease to 304 and 238 nM, respectively, suggesting a highly cooperative ternary complex formation between BTK, CRBN, and the small molecules (**Figure 2B**), while CRBN/DDB1 alone shows some weak but distinguishable basal binding affinity with BTK (**Figure S3**). Moreover, both PS-2 and PS-10 exhibit a strong binding affinity for CRBN/DDB1 complex, with binding enhanced ~5-fold in the presence of BTK (**Figure 2C**), demonstrating cooperative interactions between BTK and CRBN.

To corroborate the ternary complex formation, we labeled BTK and CRBN/DDB1 with terbium and Alexa Fluor 488, respectively (**Figure 2D**), and titrated PS-2 and PS-10 to confirm the formation of ternary complexes. PS-10 induces more ternary complex formation than PS-2, while 5 μM ibrutinib could abolish the formation of ternary complexes (**Figure 2E**), and PS-2/10 required one hour to reach the maximum concentration of the ternary complex (**Figure S4**). Collectively, the unappreciable BTK binary binding, the enhanced BTK binary binding in the presence of CRBN/DDB1, together with the BTK-CRBN ternary complex formation demonstrate the molecular glue-like behaviors of PS-2 and PS-10 [10].

BTK is a cereblon neosubstrate without G-Loop degrons

As a well-known kinase neosubstrate for CRBN, CK1α contains the canonical G-loop degron (PDB: 5FQD). Mutation of Gly40 to Asn in the G-loop of its kinase domain completely abolishes CK1α degradation induced by lenalidomide [3]. We attempted to align the kinase domain of BTK to CK1α and found a putative β-hairpin G-loop containing G423 on the N-lobe of BTK kinase domain in proximity to G40 in CK1α (**Figure S5**). Surprisingly, introduction of G423N mutation on the BTK kinase domain did not abolish its degradation induced by PS-2 or PS-10 (**Figure 3H**), suggesting an alternative non-G-loop degron mechanism.

To pinpoint the binding mode of PS-10 to BTK, we applied an irreversible BTK inhibitor ibrutinib to block the BTK ATP binding site and found that the BTK degradation induced by PS-10 is completely reversed in the presence of 1 μM of ibrutinib, demonstrating that PS-10 binds to the ATP binding pocket in BTK instead of

other allosteric sites (**Figure 1C**). When applying PS-W (the warhead-like part of PS-2/PS-10, **Figure 1A**) to compete PS-2 for BTK degradation, 500-fold excess of PS-W can only restore about 50% of BTK degradation (**Figure 2F**), demonstrating the strong affinity of BTK CRBN ternary complex induced by PS-2. In the same PS-W competition experiment with PS-10, 500-fold excess of PS-W barely rescues BTK degradation (**Figure 2G**), consistent with the fact that PS-10 forms a more stable ternary complex than PS-2.

Ternary complex structure of BTK-PS-10-CRBN

To further understand the structure of ternary complexes induced by BTK degraders, we attempted to use cryo-EM to solve the ternary complex structures for PS-2, PS-10 and NX-2127. Under our cryo-EM conditions, only PS-10 forms a stable ternary complex, whose structure is further refined to 3.42 Å resolution (**Figure 3A**).

The ternary complex structure for BTK-PS-10-CRBN showed that the tri-tryptophan pocket of CRBN and the major kinase pocket of BTK face each other, with one PS-10 molecule showing clear electron density bridging both pockets (**Figure 3B**). BTK and CRBN form very extensive protein surface interactions, burying ~1,625 $Å^2$ surface area on CRBN (**Figure S6**), distinct from the previously reported ternary complex structures of CRBN and its neosubstrates. The major PPI interface on BTK locates at the β1-strand on the N-lobe and αD-helix on the C-lobe. There are five key interactions: one salt bridge (BTK K420: CRBN D149) and four hydrogen bonds (BTK K406: CRBN G151; BTK E488: CRBN Y355; BTK M489: CRBN Q86; BTK E407: CRBN S375) (**Figure 3C-E**). The hydrogen bond between BTK M489: CRBN Q86 involves backbone hydrogen bond interactions. In addition, the pomalidomide-moiety of PS-10 adopts a novel conformation in the CRBN tri-tryptophan pocket compared with other reported pomalidomide-containing ligand conformations. Specifically, PS-10 phthalimide O gained a hydrogen bond interaction with the N atom on the W400 side chain, with a 1.5-2.0 Å translation of PS-10 pomalidomide from the classic binding position (highlighted with a green arrow in **Figure 3F**). Another feature for PS-10-bound CRBN is the introduction of two novel hydrogen bonds with CRBN N351 on the linker oxygen atoms (**Figure 3B**). Such interactions are induced by PS-10, since N351 side chain undergoes significant flipping compared with other pomalidomide-binding CRBN structures (**Figure 3G**) [32] On the BTK side, the only observable protein-ligand interaction is a hydrogen bond between pyrimidine nitrogen and the backbone nitrogen of BTK A478 (**Figure 4A**). However, we observed a novel conformation of the BTK kinase domain, with a slight rotation of the N-lobe relative to the C-lobe,

resulting in a 2.4–4.9 Å displacement of the β1 strand backbone (**Figure S7A, B**). Comparison with the currently deposited 139 PDB structures of the BTK kinase domain suggest that the original positions of the L405 side chain and the E407 backbone C=O could cause steric clashes with CRBN residues I152 and H353 (**Figure S7C**). Thus, the small-angle rotation of the BTK N-lobe likely serves as an induced-fit adaptation to resolve these clashes, facilitating BTK's accommodation on CRBN as a neosubstrate.

To investigate the role of protein-protein interface residues in PS-10-induced degradation, we conducted a mutagenesis study based on the cryo-EM structure (**Figure 3C-E**). Surprisingly, most single mutations on the protein-protein interaction (PPI) interface residues did not significantly affect the degradation potency of PS-2 or PS-10, with one exception of the K420A mutation (**Figure 3I**, **Figure S8**). However, when K420A was present, the introduction of additional interfacial mutations—such as K406A and E407A—further diminished the degradation potency of both compounds. These findings suggest that BTK-CRBN complex formation is dependent on a broad interaction network at the BTK-CRBN interface, even though individual residues may have only modest contributions.

In addition, the structure-activity relationship of PS-2 and PS-10 analogs is consistent with the binding mode of PS-10 in the ternary complex (**Figure 4A-C**). Cryo-EM structure shows that the carbonyl group (position X is C=O) in amide serves as H-bond acceptor with CRBN N351. Replacing the carbonyl with methylene reduces the activity by >10 folds (PS-2 vs PS-13, **Figure 4D**). At position Z, the carbonyl group in PS-10 serves as a H-bond acceptor with CRBN W400. Replacing the carbonyl group with a methylene reduces the activity by >40 folds (PS-2 vs PS-16; PS-10 vs PS-22, **Figure 4D**). At positions Y and Q, oxygen and nitrogen are usually associated with higher potencies, respectively (Y: PS-2 vs PS-10; Q: PS-2 vs PS-29, **Figure 4D**). At position R, replacing nitrogen with a methylene reduces the potency by ~90 folds (PS-2 vs PS-32, **Figure 4D**), indicating a planar sp^2 N atom is geometrically favored as a linker than a tetrahedral sp^3 C. Based on all the SAR knowledge, we designed PS-31 as the most potent BTK molecular glue, with DC_{50} 1.3 nM and D_{max} 98% (**Figure 4D**). Collectively, our mutagenesis studies and structure-activity relationship of PS-2/PS-10 analogs corroborate with our solved cryo-EM structure.

PS-10 bypasses BTK drug resistance and achieves brain penetration

Drug resistance is a common problem for patients on BTK inhibitors, both covalent and noncovalent inhibitors, due to the development of BTK mutations [23,33]. All these mutations are inside or close to the ATP binding

pocket, either sterically block the inhibitor access to the pocket or loss of key residues that form interactions with the inhibitors. Molecular glues typically rely on a small degron on the target protein, like G-loop in GSPT1 and CK1α, instead of strong binding in a well-defined binding pocket. We therefore hypothesize that our PS-10 can overcome BTK clinical mutations in the ATP binding pocket.

Mutational experiments demonstrated that PS-10 can efficiently degrade common BTK clinical mutations (C481X, M437R, T474I, L528W, T316A) except for two residues inside the ATP binding pocket: V416L only showing partial degradation, and A428D showing no detectable degradation (**Figure 5A**). Based on our Cryo-EM structure (**Figure 3B, 4A**), both V416 and A428 are in close vicinity to PS-10. In addition, it should be noted although BTK and CRBN form four hydrogen bonds and one salt bridge in the ternary complex structure, the energy contribution of each interaction is small to the stability of the ternary complex, as we found that single mutation on BTK at the interfacial residues barely reduces the potency of PS-2 (**Figure 3I, Figure S8**). However, the multivalent effect of the five weak interactions leads to a substantial μM basal interaction between BTK and CRBN (**Figure S3**). Therefore, we speculate that BTK molecular glues could be less prone to BTK mutations at the protein-protein interface as single mutation may not abolish the molecular glue potency.

PS-10 overcomes common clinical BTK mutations while retaining potent BTK degradation capability. TMD8-WT (wild type), TMD8-C481S, and TMD8-T474I cells were treated with different concentrations of PS-2 and PS-10 for 24 hours, followed by Western blot analysis to quantify the total BTK levels. Consistent with BTK degradation result in Ramos cells, PS-10 could induce efficient BTK degradation in TMD8-WT cells. Moreover, some common clinical BTK mutants, BTK-C481S and BTK-T474I, can also be degraded by PS-10 in a dose-response manner, while still maintaining strong degradation potency (**Figure 5C**). Furthermore, PS-2 and PS-10 demonstrate effective cytotoxic activity across TMD8 cell lines, independent of mutation status (**Figure 5D**).

NX-5948, a clinical stage BTK degrader developed by Nurix Therapeutics, showed BTK degradation in the brain, opening exciting future opportunities to apply degraders in CNS diseases [25]. Due to the small molecular weights, BTK molecular glues achieve up to 8-fold more brain penetration in a head-to-head comparison with NX-5948 (**Figure 5B**), offering a unique niche for clinical applications.

Expanding the CRBN neosubstrate scope

To explore if other kinases can be degraded by PS-10 via a similar molecular glue mechanism, we performed global proteomics of PS-10 in BTK expressing Ramos cells. Besides BTK, we found substantial protein degradation of CSK, LIMK1, TEC and AURKA in Ramos cells (**Figure 6A**), which are further corroborated with Western blot (**Figure 6B, D, S12**). The degradation of CSK and TEC are further confirmed by immunoblots showing dose-dependent degradation (**Figure 6B, D**). The protein degradation induced by PS-10 can be reversed by co-treating the Ramos cells with the corresponding ATP-pocket kinase inhibitors (**Figure 6B-E**), suggesting that similar to BTK, PS-10 also binds to the ATP binding pocket of the two tested kinases to form ternary complexes for degradation. Similar to BTK, PS-10 shows no appreciable affinities for CSK or TEC (**Figure 6G**) but induces substantial formation of ternary complexes between these kinases and CRBN/DDB1 (**Figure 6F**). Sequence alignment across all the degraded kinases reveals a dichotomy (**Figure S11**). The BTK residues that hydrogen-bond with CRBN (K406, E407, K420, E488, M489) are not conserved in CSK, LIMK1, TEC or AURKA, whereas the ATP-pocket residues contacting PS-10 are highly conserved, including V416 and A428, the two positions whose mutation impairs or abolishes BTK degradation (**Figure 5A**). This indicates that the target scope of PS-10 is dictated by compatibility with the kinase ATP pocket rather than by a conserved CRBN-binding motif: the warhead determines which kinases are recruited, while each kinase engages CRBN through its own distinct set of interface contacts.

To further explore the PS-10-CRBN ternary complex structures for the other kinase targets, we performed MD simulations to optimize the protein-protein interactions by assuming other kinases adopt similar conformations to our solved ternary complex structure for BTK. The MD and MM-PBSA results reveal several potential residues that could be involved in the protein-protein interface within the kinase-PS-10-CRBN complex (**Figure S9-S10**). We assessed these predicted interfaces by introducing point mutations across the various kinases and evaluating their impact on PS-10-induced degradation (**Figure S13**). Evaluating these mutants revealed that while some substitutions did not alter degradation, others could effectively up- or down-tune the overall potency of the degrader. This modulation of degradation activity confirms that these specific residues are actively engaged in the protein-protein interface, thereby substantiating our computational models.

Discussion

The serendipitous discovery of PS-10 as a potent BTK molecular glue challenges the conventional paradigms of targeted protein degradation and expands the structural rulebook for cereblon (CRBN) neosubstrates [8,18]. While the field has largely relied on high-affinity ligands to design PROTACs or restricted molecular glue strategies to G-loop containing proteins, our characterization of PS-10 demonstrates that efficient degradation can be achieved with negligible binary affinity for a kinase target lacking the canonical G-loop. With a DC_{50} in the single-digit nanomolar range and a D_{max} exceeding 95%, PS-10 underscores the primacy of cooperative ternary complex formation over binary binding strength, offering a compelling blueprint for targeting the undruggable kinome.

The defining feature of PS-10 is its mechanism of action, which is distinct from both traditional PROTACs and classical IMiDs [10]. Unlike PROTACs, which tether two high-affinity ligands, PS-10 acts as a true molecular glue, possessing no appreciable affinity for BTK in isolation. Its potency is derived entirely from the highly cooperative formation of a ternary complex (EC_{50} = ~200 nM, **Figure 2B**) in the presence of CRBN. This observation confirms that silent scaffolds—those appearing inactive in binary target engagement assays—could serve as potent degraders even for kinases with deep binding pockets, provided they induce sufficient E3-mediated cooperativity [7].

Structurally, the PS-10-mediated complex represents a departure from the canonical G-loop recognition motif observed in other CRBN neosubstrates such as CK1α, GSPT1, and Ikaros family proteins. Our cryo-EM analysis reveals that BTK lacks the invariant glycine degron and instead engages CRBN through an extensive protein-protein interface (~1,625 $Å^2$) involving β1-strand on the N-lobe and αD helix on the C-lobe. This interaction is stabilized by a distinct conformational plasticity in BTK, where the N-lobe rotates relative to the C-lobe to resolve steric clashes and optimize contact residues (K420, K406, E488). This induced-fit adaptation suggests that kinase neosubstrates do not require a pre-existing rigid degron but can undergo structural remodeling to accommodate the ligase. Crucially, this implies that predictive computational strategies relying on surface pattern matching, such as MaSIF-seed [11,34], must incorporate conformational ensembles rather than static structures; otherwise, valid neosubstrates capable of this remodeling may be overlooked. Indeed, our co-folding-based GluePlex workflow [14] failed to predict the PS-10-induced BTK–CRBN ternary complex, likely because Boltz2 template-based co-folding does not account for the induced-fit conformational change of BTK. This remarkable structural plasticity is further underscored by our proteomic and mutagenesis profiling of CSK, LIMK1, TEC, and AURKA. Despite lacking conserved interface residues,

all four kinases can be effectively degraded, demonstrating that productive E3-neosubstrate PPIs can be dynamically achieved through multiple distinct structural trajectories. Consequently, the potential target space for molecular glues is likely far larger than the subset of proteins containing accessible G-loops. Furthermore, the existence of a weak target binder—even one initially deemed therapeutic or biophysically inactive—presents a distinct opportunity to engineer a potent molecular glue by exploiting the plastic PPI interface nearby to maximize cooperativity, providing a novel and generalizable blueprint for rational degrader design.

While this manuscript was in preparation, CRBN molecular glues were reported for two further kinases — CDK2, recruited by the quinazolinone–glutarimide B11 (PDB 23SR) [35], and ALK, recruited by the benzoxazolone–glutarimide TRI-611 (PDB 9XZG) [36], which, together with CK1α and the PS-10 complex described here, define four structurally distinct ways of presenting a kinase domain to CRBN (**Figure 7**). The ligase side of these complexes is essentially invariant: all four glues are glutarimide-class binders occupying the same tri-tryptophan pocket, and all four kinases converge on the same CRBN surface (N351, H353, Y355, H357, E377, W386, V388 and H397). What differs is which face of the kinase fold is offered to it (**Figure 7A–D**). BTK engages through an N-lobe β1 strand (F404–L408) together with αD (N484–R490), a composite surface that presents no glycine-bearing turn, that becomes competent only after the induced-fit N-lobe rotation described above, and that is anchored by one salt bridge (K420–CRBN D149) and four hydrogen bonds (K406–G151, E407–S375, E488–Y355, M489–Q86) (**Figure 7A, E**). CK1α takes the canonical route, inserting its β-hairpin G-loop (I35–E41) into the CRBN–IMiD interface, with G40 the invariant degron glycine whose mutation abolishes lenalidomide-induced degradation [3] (**Figure 7B, E**). CDK2 instead buries an extended αC-helix and catalytic-loop face centered on Glu57, a recruitment mode reported to bypass both the canonical G-loop and the kinase glycine-rich loop [35] (**Figure 7C, E**). ALK dispenses with the N-lobe altogether, docking through a C-lobe αH–αI surface distal from the kinase active site [36] (**Figure 7D, E**). Mapped onto the folds themselves (**Figure 7E**), the four buried patches share neither position nor size (CDK2 buries roughly twice the area of the other three), yet each supports efficient degradation. Degron competence is therefore a property of the assembled ternary complex rather than of a sequence motif, and a template search built on static G-loop geometry would have recovered only one of these four. From a therapeutic perspective, recent clinical updates reinforce BTK degrader as a therapeutic direction, with NX-5948 and BGB-16673 demonstrating 76–90% overall response rates in heavily pretreated patients across CLL and Waldenström macroglobulinemia [25–27]. PS-10 offers distinct advantages over existing BTK-targeting inhibitors. By bypassing the requirement for strong occupancy of the ATP-binding pocket, PS-10 retains efficacy against

high-profile resistance mutations, including C481X and T474I, which plague covalent and non-covalent inhibitors, respectively. Notably, A428D has recently emerged as a pan-resistant residue that defeats clinical BTK inhibitors and degraders alike [37]. This is consistent with our structural observation that A428 lies in close proximity to the PS-10 binding site, where the A428D substitution likely introduces steric or electrostatic clashes that disrupt binary target engagement. Furthermore, the physicochemical properties of PS-10—specifically its lower molecular weight compared to traditional PROTACs—translate into superior tissue distribution. Notably, PS-10 achieves significantly higher brain penetration than the clinical-stage degrader NX-5948 in head-to-head comparisons, positioning PS-10-like glues as promising candidates for treating CNS lymphomas or multiple sclerosis, where blood-brain barrier penetrance is a critical bottleneck.

The extension of PS-10's activity to other kinases, including CSK, AURKA, LIMK1, and TEC, indicates that this G-loop independent mechanism is not unique to BTK. This observation paves the way for a rational design strategy moving forward. Rather than optimizing target affinity, future campaigns could focus on hinge-binding scaffolds that maximize surface complementarity with CRBN [38]. By utilizing the computational workflow and structural insights established here—specifically the role of linker rigidity and interface residues—it may be possible to systematically convert weak kinase inhibitors into potent, selective molecular glues. Ultimately, PS-10 serves as a proof-of-concept that the requirement for high-affinity ligands is not absolute, opening new avenues to degrade proteins previously deemed intractable.

Method

Cell culture

HeLa, Mino, and Ramos cells were obtained from the American Type Culture Collection (ATCC, Cat. No. CCl-2, CRL3000 and CRL1596). BTK-HiBiT Ramos was obtained from Promega. TMD8 WT and TMD8 C481S cells were shared by Dr. Jennifer Woyach at Ohio State University. Both cell lines were cultured in RPMI 1640 medium (Corning, 10-040-CV) supplemented with 10% fetal bovine serum (Corning, 35-011-CV) and 1% Pen/Strep (Thermo Fisher Scientific, Cat. No. 15140163). HeLa cells purchased from ATCC were maintained in DMEM (Corning, 10-013-CV) with 10% fetal bovine serum and 1% Pen-Strep. Cells were grown at 37 °C with 5% CO_2. For bioluminescence-based assay, phenol red-free RPMI 1640 (Gibco, 11835-030) and DMEM (Corning, 17-205-CV) were used.

HiBiT-based endpoint and protein degradation assays

For endpoint assays, BTK-HiBiT knock-in Ramos cells or HeLa cells transfected with BTK-HiBiT-RR were plated in white opaque 96-well plate (Corning, 3917) at a density of 20,000 cells per well in either 100 µL of phenol red-free RPMI 1640 medium (Ramos cells) or 100 µL of phenol red-free DMEM medium (HeLa cells), both supplemented with 10% FBS. After settling down overnight, cells were incubated with serially diluted BTK degrader compounds with the concentrations used in the text for 24 h. For degradation kinetics experiments, bioluminescence was measured after degrader incubation at different time points (1, 2, 4, 8, 24, 48 hours). Nano-Glo luciferase assay substrate was 1:100 diluted in 2× nLuc lytic buffer (100 mM MES pH 6.0, 1 mM CDTA, 0.5% (v/v) Tergitol, 0.05% (v/v) Antifoam 204, 150 mM KCl, 1 mM DTT, and 35 mM thiourea) containing 200 nM LgBiT protein to make 2× nLuc substrate lytic buffer. 100 µL 2× buffer was subsequently added into each 96-well. After brief shaking and waiting 5 min for complete cell lysis and equilibration, the luminescence signals were collected.

Immunoblotting

Mino, Ramos and TMD8 cells were seeded into the wells of six-well plates at the density of 5×10^5 cells per mL in 2 mL of complete RPMI-1640 culture medium. After overnight adaptation, cells were treated with serially diluted compounds for 24 h. After completion of treatment, whole cell lysates for immunoblotting were prepared by pelleting cells at 4 °C and 200g for 5 min. The resulting cell pellets were washed once with ice cold PBS and lysed in 1x RIPA lysis buffer (Alfa Aesar, Cat. No. J62524) supplemented with protease and phosphatase inhibitor cocktail (Thermo Fisher, Cat. No.78430). Lysates were centrifuged at 15,000g for 10 min at 4 °C and protein concentrations were assessed using BCA assay (Pierce, Cat. No.23225). Same amounts of protein for each sample were loaded onto sodium dodecyl sulfate-polyacrylamide gel, separated by electrophoresis (Bio-Rad) at 120 V for 1.5 h and transferred to PVDF membrane using a Transblot Turbo system (Bio-Rad). After blocking for 2 h at room temperature in 4% BSA-TBST, the membranes were immunoblotted with the specified primary antibodies at the dilution of 1:1000 in TBST (Cell Signaling Technology: anti-BTK Cat. No.8547, anti-IKZF1 Cat. No.14859, anti-IKZF3 Cat. No.15103, anti-β-actin Cat. No.4570, anti-LIMK1 Cat. No.3842, anti-Aurora A Cat. No. 14475, anti-CSK Cat. No.4980; anti-Tec was perched from Abclonal Cat. No. A22074) overnight at 4 °C, and the HRP conjugated secondary antibodies (Cell Signaling, Cat. No.7074, 1:1000 in TBST) for 1 h at room temperature. Imaging was performed using

the ECL Prime chemiluminescent Western blot detection reagents (Kindle Biosciences, Cat. No. R1100) by visualization of the blots with an Imager (Kindle Biosciences, Cat. No. D1001). All western blots were subsequently processed and quantified with Imager software ImageJ and protein level was normalized to the β-actin loading controls.

AlamarBlue cell viability assay

TMD8 or Mino cells were plated into the wells of 96-well plates (Corning, Cat. No.3598) at the density of 6×104 cells per mL in 100 μL of complete RPMI-1640 culture medium. After overnight recovery, cells were exposed to serially diluted BTK PROTAC compounds (from 10,000 to 0.64 nM, 5-fold dilution) for 72 h, which was followed by adding pre-warmed Resazurin sodium (Sigma, Cat. No. 199303) solution (1 mg mL−1 in PBS) in an amount equal to 10% of the volume in the well. Four hours after incubation, fluorescence signals were collected with a BioTek SYNERGY H1 microplate reader at excitation/emission 544/590 nm from top with gain at 60. The IC_{50} was calculated using GraphPad Prism software with a four-parameter dose response curve fit.

Degradation competition assay

BTK-HiBiT Ramos cells were pre-incubated with indicated inhibitors for 1h, then cells were plated in white opaque 96-well plate at a density of 20,000 cells per well in 100 μL of phenol red free RPMI 1640 medium. Then cells were incubated with serially diluted BTK degrader compounds with the concentrations used in the text for 4 h. Nano-Glo luciferase assay substrate was 1:100 diluted in nLuc lytic buffer (100 mM MES pH 6.0, 1 mM CDTA, 0.5% (v/v) Tergitol, 0.05% (v/v) Antifoam 204, 150 mM KCl, 1 mM DTT, and 35 mM thiourea) containing 200 nM LgBiT protein to make 2× nLuc substrate lytic buffer. 100 μL 2× buffer was subsequently added into each 96-well. After brief shaking and waiting 5 min for complete cell lysis and equilibration, the luminescence signals were collected.

TR-FRET binary biochemical binding assays

Time-resolved fluorescence resonance energy transfer (TR-FRET) assay was carried out to evaluate the binding of indicated compounds and BTK or CRBN by competition with a BODIPY-FL labeled BTK/CRBN tracer.

For binary binding with BTK without the presence of CRBN: The assay was performed in 10 μL assay buffer (50 mM Tris, pH7.5, 0.1% Triton X-100, 0.01% BSA, and 1 mM DTT) with 0.3 nM (400X from storck solution) Tb-anti-MBP (Revvity, Cat.No. 61HI2TLB), 2 nM MBP-BTK, 120 nM BTK-BODIPY tracer and serial diluted compounds (from 100000 nM, 2-fold dilutions) in opaque 384well plates. The assay mixtures were incubated at room temperature in dark for 3 min, unless specified otherwise, and the signals were collected using a PheraStar microplate reader (BMG Labtech) to measure the time-resolved fluorescence emission ratio (F520 nm/F490 nm) of each well every 6 min. Raw data from the plate reader at 1h were used directly for analysis. The curve-fitting software GraphPad Prism 10 was used to generate graphs and curves and to determine IC_{50} values. According to Cheng-Prusoff equation, K_d values equal to $IC_{50}/2$, since the tracer concentration in this assay is at tracer's IC_{50} value against MBP-BTK.

For binary binding with BTK with the presence of CRBN: Incubate the compounds and CRBN/ His-DDB1ΔB protein at the concentration ratio at 5:1 for 30 min in advance, then dilute them 2-fold and add them to the same reaction system as above. CRBN-compound complex concentration was calculated according to equilibrium equation [CRBN-compound] = [CRBN][compound]/K_d, where the K_d value was obtained from the following paragraph “binary binding with CRBN without the presence of BTK”. The calculated CRBN-compound complex concentrations were used in plotting.

For binary binding with CRBN without the presence of BTK: The assay was performed in 10 µL assay buffer (50 mM Tris, pH7.5, 0.1% Triton X-100, 0.01% BSA, and 1 mM DTT) with 0.3 nM (400X from stock solution) Tb-anti-His (Revvity, Cat.No. 61MBPTAA), 2 nM CRBN/His-DDB1ΔB, 125 nM Thalidomide-BODIPY tracer and serial diluted compounds (from 100000 nM, 2-fold dilutions) in opaque 384well plates. The assay mixtures were incubated at room temperature in dark for 3 min, unless specified otherwise, and the signals were collected using a PheraStar microplate reader to measure the fluorescence emission ratio (F520 nm/F490 nm) of each well every 6 min. Raw data from the plate reader at 1h were used directly for analysis. The curve-fitting software GraphPad Prism 10 was used to generate graphs and curves and to determine IC_{50} values. According to Cheng-Prusoff equation, K_d values equal to $IC_{50}/2$, since the tracer concentration in the assay is at tracer’s IC_{50} value against His-CRBN/DDB1.

For binary binding with CRBN with the presence of BTK: Incubate the compounds and full length of BTK protein at the concentration ratio at 1:1 for 30 min in advance, then dilute them 2-fold and add them to the same reaction system as above.

TR-FRET ternary biochemical binding assays

Time-resolved fluorescence resonance energy transfer (TR-FRET) assay was carried out to evaluate the binding of indicated compounds and BTK or CRBN. The assay was performed in 20 µL assay buffer (50 mM Tris, pH7.5, 0.1% Triton X-100, 0.01% BSA, and 1 mM DTT) with 0.3 nM (400x from stock solution) Tb-anti-MBP (Revvity, Cat.No. 61MBPTAA), 5 nM MBP-BTK, 100 nM CRBN/His-DDB1ΔB and 200nM HIS Lite™ OG488-Tris NTA-Ni complex (AAT Bioquest, Cat No. 12615), serial diluted compounds (from 100 uM, 2-fold dilutions) in opaque 384 well plates: Incubated 5 nM MBP-BTK full length protein with Tb-anti-MBP for 30 minutes, incubated CRBN/His-DDB1ΔB with Tris-NTA-Ni for 30 minutes. After incubation, the two labeled protein solutions were mixed, and a mixture (10 µL/well) of the reagents was dispensed into a 384-well plate, then compound was dispensed with Pico 8. The assay mixtures were incubated at room temperature in dark for 3 min, unless specified otherwise, and the signals were collected using a CLARIOStar microplate reader (BMG Labtech) to measure the fluorescence emission ratio (F520 nm/F490 nm) of each well every 6 min. Raw data from the plate reader at 1h were used directly for analysis. The curve-fitting software GraphPad Prism 10 was used to generate graphs and curves.

For CSK (Cat: C63-10G-10, Lot: A1171-4, SignalChem) and Tec (Cat: T03-10G-10, Lot: O3817-4, SignalChem), protein was used as received from commercial sources without further purification. Tb-anti-GST (Revvity, Cat.No. 61GSTTLA, LOT. 17AR) was used instead of Tb-anti-MBP. The reagent concentrations and experimental settings are consistent with those used for BTK TRFRET ternary assay.

Plasmid cloning & mutagenesis

The plasmid cloning for high throughput BTK full length or kinase domain degradation assay (pcDNA3.1-BTK-HiBiT-RR) has been previously described [39]. The genes encoding kinase domains of CSK (188-450), TEC (360-631), LIMK1 (329-637), and AURKA (122-403) in-frame with the C-terminal HiBiT-RR tag were synthesized by Viva Biotech and cloned into the pcDNA3.1 plasmid. Site-directed mutagenesis was performed using ClonExpress II One Step Cloning Kit (C112, Vazyme) according to the protocol from the manufacturer. Mutations are verified by Sanger sequencing. The DNA primers for cloning are listed in **Table 1**.

Table 1. The mutagenesis primers used in this study.

Primer name	sequence	Primer name	sequence
BTK_T316A-F	GGCAAATATGCAGTGTCTGTGTTTG	TEC_E375A_F	TTATGAGGGCGCTGGGCAGCG
BTK_T316A-R	AGACACTGCATATTTGCCAGCTTTGC	TEC_E375A_R	GCCCAGCGCCCTCATAAAGGT
BTK_K406A-F	CTTCTTGGCGGAGCTGGGGACTGGAC	TEC_R385A_F	GAGTGGTGGCGCTGGGAAAATGG
BTK_K406A-R	CCCAGCTCCGCCAAGAAGGTCAGG	TEC_R385A_R	TCCCAGCGCCACCACTCCG
BTK_E407A-F	TTGAAGGCGCTGGGGACTGG	TEC_Q456A_F	CTGAGGGCGAGACAGGGCC
BTK_E407A-R	CAGTCCCCAGCGCCTTCAAGAA	TEC_Q456A_R	CCCTGTCTCGCCCTCAGAAAATTCAG
BTK_V416L-F	GGGGTACTGAAGTATGGGAAATGGA GAGG	TEC_H460A_F	AGGGCGCCTTTAGCAGAGACG
BTK_V416L-R	CCCATACTTCAGTACCCCAAATTGT	TEC_H460A_R	TCTGCTAAAGGCGCCCTGTCTCT
BTK_K420A-F	AGTATGGGGCATGGAGAGGCCAGTA CG	TEC_N571A_F	TACACCGCCTACGAGGTGGTGACAAT
BTK_K420A-R	CCTCTCCATGCCCCATACTTCACTACCC	TEC_N571A_R	ACCTCGTAGGCGGTGTATTTCTCAAAAG G
BTK_G423N-F	AATGGAGAAACCAGTACGACGTGGC	CSK_K203A_F	ATCGGTGCGGGTGAGTTCGGTGACGTGA TGCT
BTK_G423N-R	CGTACTGGTTTCTCCATTTCCCATACTT CAC	CSK_K203A_R	AACTCACCCGCACCGATGGTCTGCAGCA GCT
BTK_A428D-F	CGACGTGGACATCAAGATGATCA	CSK_K218A_F	TGGTAACGCCGTTGCCGTTAAGTGCA
BTK_A428D-R	CATCTTGATGTCCACGTCGTACTGG	CSK_K218A_R	ACGGCAACGGCGTTACCACGG
BTK_M437R-F	GGCTCCAGGTCTGAAGATGAATTCA	CSK_R283A_F	TTCTCGTGGTGCTTCTGTGCTGGG
BTK_M437R-R	ATCTTCAGACCTGGAGCCTTCTTTGAT	CSK_R283A_R	ACAGAAGCACCACGAGAACGCAG
BTK_T474I-F	TTCATCATCATCGAGTACATGGCCAAT GGC	CSK_S284A_F	TCGTGCTGTGCTGGGCGGTGACTGTCT
BTK_T474I-R	ATGTACTCGATGATGATGAAGATGGG GCG	CSK_S284A_R	GCCCAGCACAGCACGACCACGAGAAC
BTK_C481F-F	AATGGCTTCCTCCTGAACTACCTGA	LIMK1_K417A_F	AGTATATTGCGGGCGGCACCCTG
BTK_C481F-R	GTTCAGGAGGAAGCCATTGGC	LIMK1_K417A_R	TGCCGCCCGCAATATACTCGGTAATGAA G
BTK_C481R-F	AATGGCCGCCTCCTGAACTACCT	LIMK1_S427A_R	GGAATCCATGGCCTTGATGATGCC
BTK_C481R-R	GTTCAGGAGGCGGCCATTGG	LIMK1_S427A_F	ATCAAGGCCATGGATTCCCAGTATCC
BTK_C481S-F	TGGCAGCCTCCTGAACTACCTG	LIMK1_D551A_F	GATCCTGCTTATCTGCCTAGGACAATGG A
BTK_C481S-R	GTAGTTCAGGAGGCTGCCATTG	LIMK1_D551A_R	AGGCAGATAAGCAGGATCGGCAT
BTK_C481W-F	AATGGCTGGCTCCTGAACTAC	LIMK1_Y552A_F	CCTGATGCTCTGCCTAGGACAATGGAT

BTK_C481W-R	GTTCAGGAGCCAGCCATTGGCC	LIMK1_Y552A_R	CCTAGGCAGAGCATCAGGATCGGC
BTK_E488A-F	TGAACTACCTGAGGGCAATGCGCCACCG	LIMK1_Y570A_F	GGATAGAGCCTGTCCTCCTAATTGCCC
BTK_E488A-R	TGCCCTCAGGTAGTTCAGGAGG	LIMK1_Y570A_R	GAGGACAGGCTCTATCCAGAAAGCCTCT
BTK_L528W-F	CTCGAAACTGTTGGGTAAACGATCAAG	AURKA_R151A_F	ATCTGGCAGCCGAAAAGCAG
BTK_L528W-R	TACCCAACAGTTTCGAGCTGCCAG	AURKA_R151A_R	GCTTTTCCGGTGCCAGATAAACATTAC
AURKA_D229A_F	GTAAATTTGCTGAACAGCGTACCGCCA	AURKA_D229A_R	GCTGTTCAGCAAATTTACTCAGTTTCTGCAG

Protein purification (BTKFL, KD, CRBN/DDB1)

His-CRBN/His-DDB1ΔB complex

Recombinant baculoviruses for the co-expression of human DDB1ΔB and CRBN were generated using plasmids generously provided by the Eric Fischer laboratory (Addgene plasmid #124213, His_6-Spy-hsDDB1ΔB, and Addgene plasmid #124214, His_6-TEV-hsCRBN). Each plasmid was co-transfected into *Spodoptera frugiperda* (Sf9) cells along with linearized wild-type baculovirus DNA following standard Bac-to-Bac procedures.

Briefly, Sf9 cells were seeded at ~1 × 10^6 cells/mL in 6-well plates and co-transfected with 10 µg of total plasmid DNA (5 µg each of His_6-Spy-hsDDB1ΔB and His_6-TEV-hsCRBN constructs) and the manufacturer-recommended amount of linearized baculovirus genomic DNA using a lipid-based transfection reagent. Transfected cultures were incubated at 27 °C for 72–96 h until signs of viral infection (e.g., cell enlargement and reduced viability) were observed. The co-transfection supernatant (P0) was collected and subjected to plaque purification to isolate individual viral clones.

Plaque assays were performed according to established protocols to ensure the isolation of homogeneous recombinant viruses. Ten individual plaques were picked, amplified in Sf9 cells (P1), and expression-tested by small-scale infection of Sf9 cultures (10 mL) at a multiplicity of infection (MOI) of approximately 0.1. After 72 h of incubation at 27 °C, infected cell pellets were harvested, lysed, and analyzed by SDS-PAGE to confirm the co-expression of His_6-Spy-hsDDB1ΔB and His_6-TEV-hsCRBN. Viral isolates that produced both target proteins at the expected molecular weights were selected for large-scale amplification to generate high-titer recombinant virus stocks (P2–P3) for protein production.

3.50 mL of hsCRBN (2.9×10^8 pfu/mL) and 3.22 mL of HisDDB (3.1×10^8 pfu/mL) baculovirus suspension was used for 500 mL co-infection of SF9 insect cells.

For DDB1 (△BPB)/ CRBN purification, the cell pellets from insect cells were resuspended in buffer D (50 mM HEPES pH7.5, 0.2M NaCl, 5mM β-mercaptoethanol, 0.1 mM PMSF, 5 % glycerol, and 1 protease inhibitor cocktail (Thermo Fisher, catalog J61852.XF) tablet), lysed by sonication and centrifuged at 20,000xg for 45 minutes at 4°C. The supernatant was passed through Nickel resin (Qiagen) pre-equilibrated with buffer D and washed with buffer E (50 mM HEPES pH7.5, 0.2M NaCl, 5mM β-mercaptoethanol, 20mM Imidazole, 5 % glycerol). The protein was eluted with buffer F (50 mM HEPES

pH7.5, 0.2M NaCl, 5mM β-mercaptoethanol, 300mM Imidazole, 5 % glycerol), concentrated to 0.5-1 mL and further purified using Superdex 200 (GE healthcare) with buffer G (50 mM HEPES pH7.5, 0.2M NaCl, 5mM DTT, 5 % glycerol).

All purified proteins were pooled, concentrated, supplemented with 30% glycerol, aliquoted, flash-froze, and stored at -80°C for further biochemical and structural studies.

MBP-BTK full length and kinase domain

The gene of human BTK was amplified from the pcDNA3-flag-BTK and inserted into a modified pLEXm mammalian expression vector (1) with an N-terminal MBP tag containing a prescission cleavage site. The plasmids expressing full length, kinase domain and/or point mutation BTK were constructed by double restriction enzyme digestion into a modified vector. All the constructions were confirmed by Sanger sequencing (Genewiz).

The HEK293T cell (American Type Culture Collection, catalog CRL-3216) were used for transfection and protein expression. For each liter of transfection, 1 mg of DNA and 40 mg fresh-made Polyethyleneimine (Polysciences, catalog 23966-1) solution (1 mg/mL) were prepared separately with Hybridoma medium (Thermo Fisher, catalog 12045084) to a final volume of 20 mL each (total 40mL of transfection mixture), filtered and incubated together for 1 hour before adding to the cell culture with density of 1.8-2.2 million cells/mL. After overnight growth, sodium butyrate (Sigma, catalog 303410-100) was added to a final concentration of 10mM to enhance the protein expression.

The cells were harvested after 48 hours of sodium butyrate addition. The cell pellets were resuspended in lysis buffer containing 50 mM HEPES pH7.5, 0.4M NaCl, 1 mM DTT, 0.1 mM PMSF, 5 % glycerol, and 1 tablet protease inhibitor cocktail (Thermo Fisher, catalog J61852.XF), lysed and centrifuged at 20,000xg for 45 minutes at 4°C. The supernatant was incubated for 2 hours with pre-equilibrated amylose resin (NEB, catalog E8021L), passed through the gravity column, washed and eluted with buffer A (50 mM HEPES pH7.5, 0.4M NaCl, 1 mM DTT, 300 mM maltose (Sigma, catalog M5885), 5 % glycerol). The eluted protein was cleaved overnight on ice using prescission protease to remove the MBP tag. The protein was dialyzed with buffer B (50 mM HEPES pH7, 0.05M NaCl, 1 mM DTT, 5 % glycerol). Next, the protein was loaded onto pre-equilibrated Mono S (Cytiva) column with buffer B. The protein was eluted from the column with the buffer C (50 mM HEPES pH7, 1M NaCl, 1 mM DTT, 5 % glycerol) using NaCl gradient. The purity of BTK proteins was assessed by SDS-PAGE and confirmed over 95%.

Computation workflow

Docking PS-10 warhead onto BTK kinase domain

The PS-10 warhead molecule was docked into the BTK kinase domain using Maestro 13.1 (Schrodinger Inc., US) to obtain the binary model. Starting from the BTK crystal structure co-crystallized with CC-292 (PDB: 5P9L) [40], Protein Preparation Workflow was used to process the structure, including filling the missing side chain, optimizing H-bond assignment, deleting water in the model and minimizing the structure in OPLS4 forcefield. The PS-10 warhead was preprocessed with LigPrep to generate possible charge state under pH 7.0±2.0. Receptor grid was defined as a 12-angstrom cubic box centered at the centroid of CC-292 in 5P9L. All charge states attempted to dock into the grid using Glide XP precision model. The docked

model with the core pharmacophore overlapping with CC-292 was used for downstream ternary complex modeling.

Molecular dynamics simulation of BTK, CSK, TEC, AURKA, LIMK1 kinase domain and MM-PBSA residue decomposition

GROMACS version 2022.1 and CHARMM36-feb2021 forcefield were used for MD simulations. For each initial set of coordinates, the periodic boundary condition was applied as follows: the box was set as cubic with absolute size of each side greater than the largest dimension of the system by 10 Å. Explicit water was added, and the system charge was neutralized with 150 mM sodium and chloride ions. A steepest descent energy minimization was performed to remove steric clashes or inappropriate geometry until the structure converged. Consecutive 100 ps NVT ensemble simulation with T at 300 K using V-rescale and 100 ps NPT ensemble simulations with T at 300 K and pressure at 1 bar with Berendsen barostat were then performed to allow temperature and pressure coupling for protein and nonprotein groups. The convergence of system temperature, pressure, and density were confirmed. Finally, the production run of 100 ns was performed. Short range van der Waals was calculated using Verlet neighbor searching algorithm with a cut-off of 1.2 nm. Coulomb was calculated using Particle Mesh Ewald and the cut-off was set as 1.2 nm. During the production run, coordinate frames were saved every 10 ps. GMX_MMPBSA was used to calculate binding free energy between CRBN and BTK and their per-residue decomposition within 4 Å of PPI using Poisson Boltzmann method (PBRadii=7). According to the MM-PBSA energy decomposition, candidate residues were picked out for in-vitro experimental validation.

For each input structure, 4 replicates of the HAPOD simulation were performed consisting of 50 ns production run with 0-10 ns temperature 300K, 10-30ns 300-400K gradient, and 30-50 ns 400K in the NPT ensemble. Trajectory RMSD for BTK was calculated when CRBN is aligned.

The MD simulations were performed on Lonestar6 server from Texas Advanced Computing Center under project CHE23001. The GROMACS was compiled with GPU-enabled code and the job was mainly run on GPU.

Global proteomics of PS-series compound degradation

Sample preparation

Ramos cells were plated in 12-well plates with each well containing 0.2 million cells and allowed to grow for 24 hours. The next day, PS compounds or equi-volume of DMSO was added into the culture medium to achieve final concentration 200 nM. After 24 hours treatment in 37 degrees, cells were collected by centrifuging at 500 rpm for 5 min. Cells were lyzed in 50 ul lysis buffer (100mM HEPES pH 8.5, 1% SDS, 1% NP-40, 1x Protease inhibitor cocktail) and the protein amount was normalized to 30 ug in 50 ul quantified by BCA assay. Reduction was performed by adding 5 ul 50mM DTT and incubate at 37 degree for 15 min, and alkylation by adding 14 ul 100mM iodoacetamide and incubate in dark for 30 min under room temperature. Then the protein samples were cleaned up using SP3 method [41,42]. Briefly, 30ug protein samples and 300ug SP3 beads (1:1 mixture of Sera-Mag Carboxylate SpeedBeads Cat. #45152105050250 and Cat. #65152105050250) were mixed. Equal volume of 100% EtOH was added to achieve 50% v/v EtOH to initiate protein binding with vigorous vortex and quick bath sonication. The

mixture was incubated with 1,000 rpm shaking for 10 min at room temperature. Supernatant was removed and the beads were washed 3 times with 80% EtOH. The beads were air dried, resuspended in 50ul 200mM HEPES pH 8.5 containing 0.6 ug trypsin/Lys-C (Promega, V5073) and incubated on a 37 degree 1,100 rpm shaker overnight.

After digestion, SP3 peptide clean-up was initialed by adding 1mL 100% ACN into the peptide-bead mixture to achieve >95% v/v. The samples were sonicated until the beads are back in suspension, followed by 10 min 1000 rpm shaking at room temperature. The SP3 beads were washed twice with 100% ACN, then air dried to remove remaining ACN. Peptides were eluted with 2% DMSO with brief sonication and incubated for 5 min on a 1000 rpm room temperature shaker. The eluted peptides were dried using SpeedVac and stored in -80˚C before LC-MS/MS analysis.

LC-MS/MS analysis

The resulting peptides were reconstituted in 5% acetonitrile with 0.1% formic acid in water, and 1500 ng was loaded in trap and elute mode using the Thermo Scientific™ PepMap™ Neo Trap Cartridge (P/N 174500) onto an Ionopticks Aurora Frontier XT 60x75 C18 UHPLC column with the Thermo Scientific™ Vanquish™ Neo UHPLC system. The sample loading, trap column washing (800 bar), and separation column equilibration (1500 bar) were performed using the pressure control features of the Vanquish Neo UHPLC system.

Buffers A and B consisted of 0.1% formic acid in water (Fisher Scientific, Optima LC-MS grade) and 0.1% formic acid/80% acetonitrile (Fisher Scientific, Optima LC-MS grade), respectively. The column was heated to 50 °C using the Ionopticks column heater (COLHTR01) and controller (IOHEATCON1). Peptides were eluted at a flow rate of 250 nL/min with an isocratic 8% buffer B over 1 minute, followed by a stepped gradient of 8%-28% buffer B over 60 minutes and 28%-50% buffer B over 17 minutes. The column was subsequently washed for 5 minutes at 99% buffer B at a flow rate of 400 nL/min at the end of the gradient.

The eluted peptides were ionized using a Thermo Scientific™ EASY-Spray™ Source and analyzed on an Orbitrap Astral MS using narrow window DIA analysis. Briefly, MS1 spectra were collected in the Orbitrap mass analyzer every 0.6 seconds at a resolving power of 240,000 at m/z 200 over an m/z range of 380–980. The MS1 normalized automated gain control (AGC) target was set to 500% (5e6 charges) with a maximum injection time of 5 ms. Precursor ions were fragmented using high-energy collisional dissociation (HCD) with 25% normalized collision energy. Fragment ions were scanned in data-independent acquisition (DIA) mode in the Astral mass analyzer over an m/z range of 380–980 with a 2 m/z isolation window. The normalized AGC target was set to 500% and the maximum injection time was set to 3.5 ms. Window placement optimization was enabled.

Data analysis

Raw data was processed using Spectronaut™ software with a directDIA™ approach, searched against the human proteome database downloaded from UniProt (January 2024). Both peptide-spectrum matches (PSMs) and proteins were filtered at a 1% false discovery rate (FDR). The resulting protein intensities table was exported and plotted using in-house python script which performs student t-test and use Benjamini-Hochberg method to correct for multiple t-test FDR.

In vivo pharmacokinetics of PS-2, PS-10, PS-29 and NX-5948

In vivo pharmacokinetic (PK) studies were performed by Pharmaron. The study was an intravenous (IV) PK analysis conducted in four animals. A single IV dose of 2.17 µmol/kg was administered. The formulation consisted of a 40%:20%:40% (wt/wt) mixture of propylene glycol, DMSO, and H_2O, with the dosing solution prepared at a concentration of 0.4 µmol/mL. For two of the animals, blood samples were collected at 0.083, 0.25, 0.5, 1, 2, 4, 8, and 24 hours post-dose. For the remaining two animals, both blood and brain samples were collected at 0.083 hours post-dose.

CryoEM Structure Determination of DDB1/CRBN/PS-10/BTK Sample preparation:

Grid vitrification

Ternary complex formation and grid vitrification protocols followed the ones previously described in [43]. Full-length DDB1/CRBN complex (Q96SW2) custom expressed and purified by Crelux GmbH was mixed with 5x molar excess of appropriately diluted 10mM DMSO PS-10 compound stock and the solution was incubated for 2 mins on ice. Subsequently, a full-length BTK complex was added to the mixture in 2:1 molar excess ratio with respect to the DDB1/CRBN complex and the solution was incubated for another 2 hours. Just prior to grid application, LMNG was added to the mixture to a final concentration of 0.011% and 3.5 µL of the final solution were applied to UltraAuFoil 300 mesh R1.2/1.3 grids (SPT Labtech) pretreated identically to [43].

Data acquisition

The selected grid was transferred under cryogenic conditions into the TFS Titan Krios 300 kV TEM with Cs 2.7 mm and equipped with XFEG. Micrographs were acquired on the Gatan K3 camera under low-dose condition with a total flux of 65 e-/Å2. Data were collected without tilt with underfocus values ranging from -0.46 µm to -2.89 µm at a nominal magnification of 165,000x, resulting in nominal resolution of 0.5113 Å/px. Automated data acquisition was done by SerialEM [44] in fringe-free imaging mode using 6x6 beam shift pattern and 4 exposures per hole in a movie-mode and 2s exposure was recorded into 40 individual frames. 14,201 collected movies were then globally and locally (6x6 patches, 20% patch overlap) aligned to compensate for drift and beam-induced motion. The resulting dose-weighted sum of aligned frames was used for subsequent image processing steps, except for estimating the contrast transfer function (CTF) parameters, which were estimated from aligned, non-dose weighted micrographs using the program ctffind4[45].

Map reconstruction and model building

Entire data processing was done using Eyen's internally modified software stack based on SCIPION 3.0.9 package [44]. The set of 14,201 dose-weighted micrographs, 4x binned, and denoised using a machine-learning protocol were used for particle picking. After extraction into a 100 x 100 pixel box there were 13,381,946 particles available for further processing.

The initial particles were subjected to four rounds of RELION [46–49] 2D classification and only particles from high-quality 2D class averages were selected, leaving a clean set of 388,541 particles. Two rounds of 3D refinement and 3D classification were applied to get initial alignment and an even cleaner set. This particle

set was then re-extracted without binning from the original micrographs leaving the final set of 365,023 particles (in 560 x 560 pixel box).

The processing continued with a focused 3D refinement using a mask around CRBN and BTK substrate since both of these subunits are flexible with respect to the dominant DDB1 subunit.

Final steps in the processing entitled improving the frame alignment using Bayesian polishing [53], followed by another 3D refinement and 3D classification without alignment, another 3D refinement and finally a CTF refinement followed by a final 3D refinement with increased tau fudge factor to 6 from 321,907 particles reaching the final resolution of 3.42 Å. The final 3D auto-refine was followed by the RELION post-processing protocol generating the final 3D volumes for model building. The post-processing used MTF-correction and manually chosen b-factor of -50.

Only the well-resolved, and relevant parts for binding mode determination, of CRBN subunit, PS-10 compound and BTK substrate were modelled. The modeling started from Eyen's internal CRBN coordinates originally created using high-resolution, 2.5 Å CryoEM maps of CRBN in a closed conformation. PDB:8s93 was used as an initial model for the BTK substrate. Initial PS-10 compound model originated from computational docking studies performed prior to the experimental structural work. These initial models were manually remodeled to correspond to the map density. The model building then proceeded iteratively, combining restrained molecular dynamics fitting with manual intervention to build stereochemically valid models with best possible correspondence to the density. Cryo-EM data collection, refinement, and validation statistics are summarized in **Supplementary Table 1**.

Data availability

The mass spectrometry raw files for DIA label-free global proteomics have been deposited in the MassIVE dataset under accession number MSV000099797 (pw: 8X48CMx2aH06b08I). Cryo-EM structure model of CRBN-PS-10-BTK^{KD} has been deposited to Protein Data Bank under accession code 9YTE. The Cryo-EM map has been deposited to EMDB under accession code EMD-73459.

Acknowledgements

pESF140_HisSpy_DDB1ΔB and pAJ075_hsCRBN were gifts from Eric Fischer lab (Addgene plasmid # 124213 and 124214).

Funding Statement

This research was supported in part by the National Institutes of Health (R01-CA250503 to J.W.), the Cancer Prevention & Research Institute of Texas (CPRIT, RP220480 to J.W.), Michael E. DeBakey, M.D., Professor in Pharmacology (to J.W.), Center for NextGen Therapeutics seed funding (to J.W.).

Competing Interests Statement

The authors declare the following competing financial interest(s): J.W. is a co-founder of Chemical Biology Probes, LLC. and serves as a consultant for CoRegen Inc. J.W. and X.Y. are co-founders of Fortitude Biomedicines, Inc. and hold equity interest in this company. R.C., H.L., X.Y., X.Q., and J.W. are the co-

inventors on a patent related to this work. J.A.W. consults for AstraZeneca, AbbVie, BeOne, Genentech, Johnson & Johnson, Loxo@Lilly, Merck, and Newave. The remaining authors declare no competing interests.

List of Figures

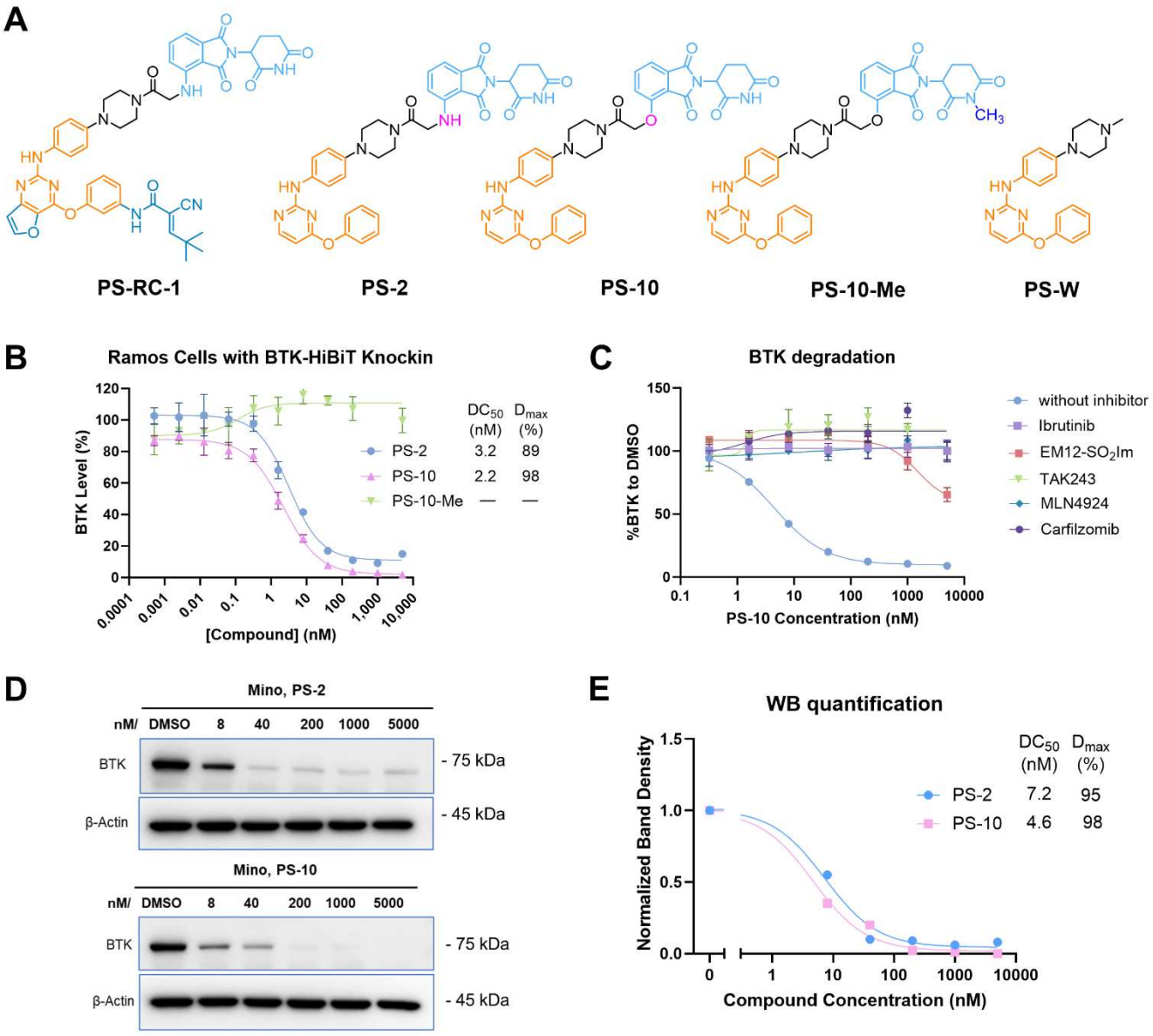


Figure 1. Identification of the minimal moiety with BTK degradation potency

A. Inspiration of PS-2 structure from PS-RC-1, its derivative PS-10, and negative control compounds PS-10-Me and PS-W. **B**. Ramos cells with endogenous BTK tagged with HiBiT were treated with serial dilution of PS-2, PS-10, and PS-10-Me for 24h. Shown are mean ± SD luminescence values normalized to DMSO-treated samples. **C**. Ramos cells with endogenous BTK tagged with HiBiT were treated with serial dilution of PS-10 in the absence or presence of 1 μM BTK inhibitor ibrutinib, 5 μM CRBN covalent binder EM12-SO_2Im [31], 1 μM E1 inhibitor TAK243, 1 μM NEDDylation inhibitor MLN4924, or 1 μM proteasome inhibitor carfilzomib for 1 hours. Shown are mean ± SD luminescence values normalized to DMSO-treated samples in the presence of other inhibitors. **D**. Immunoblots for Mino cells treated with a serial dilution of PS-2 or PS-10 for 24h. **E.** Densitometry analysis of panel D immunoblots.

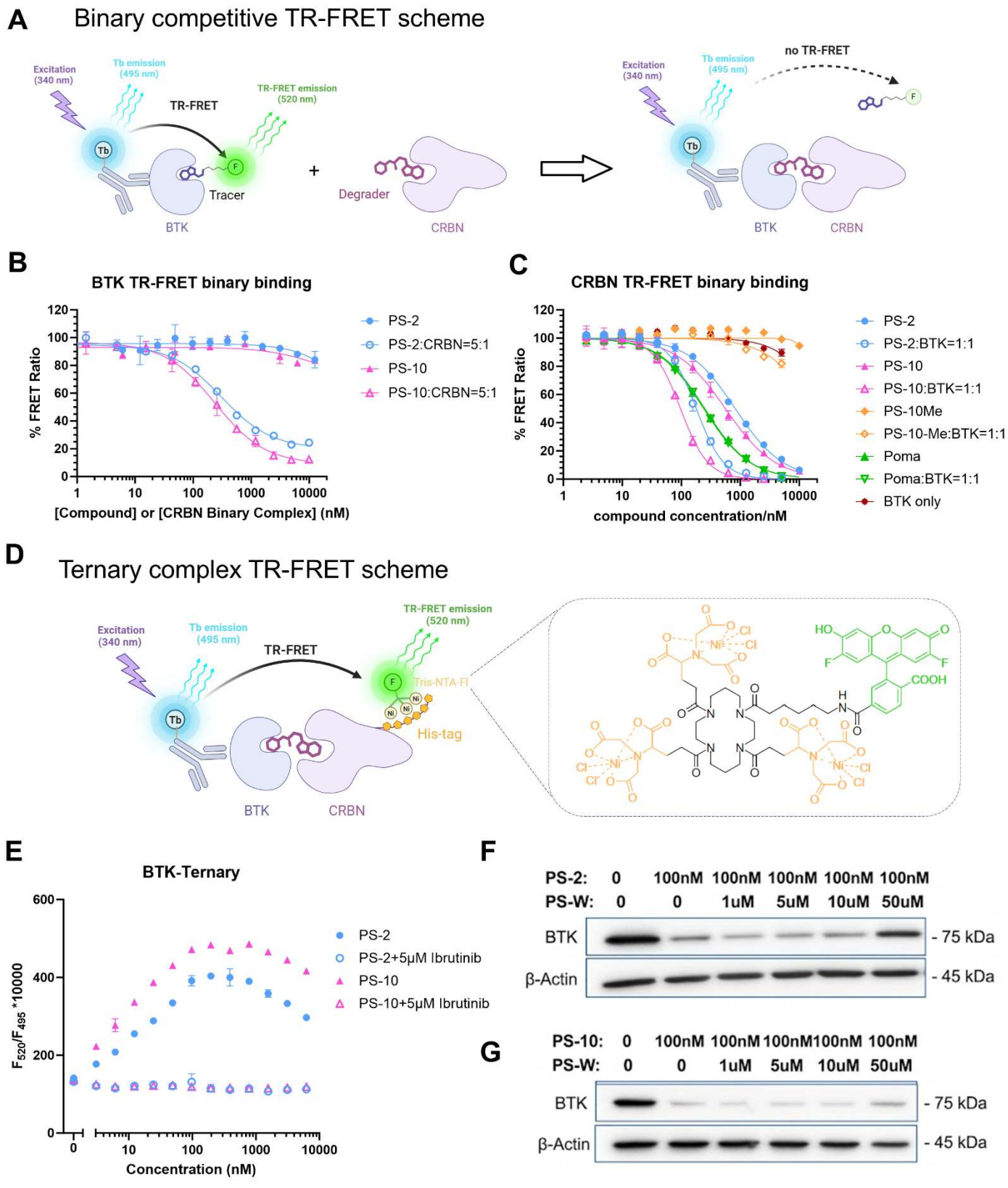
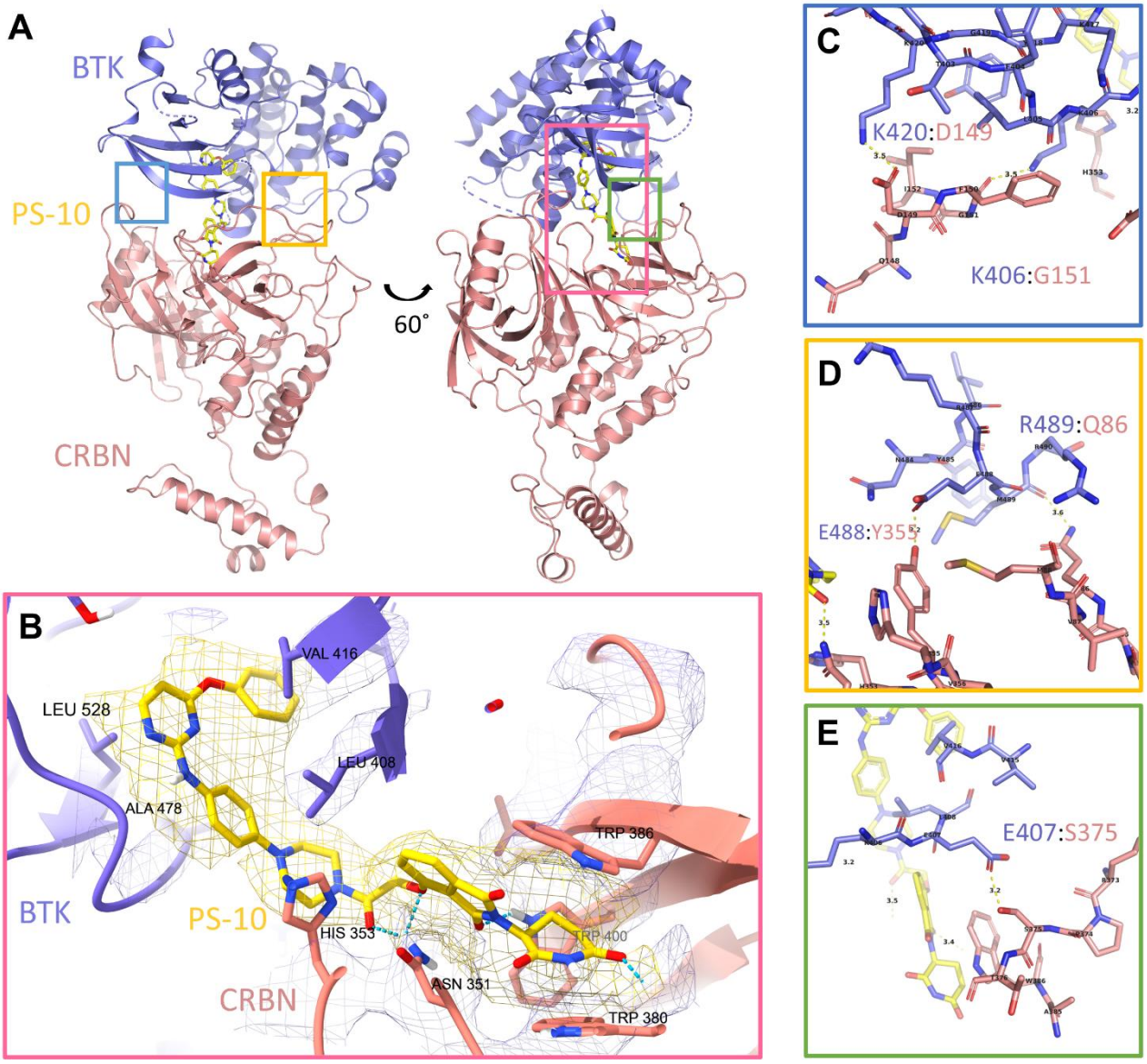
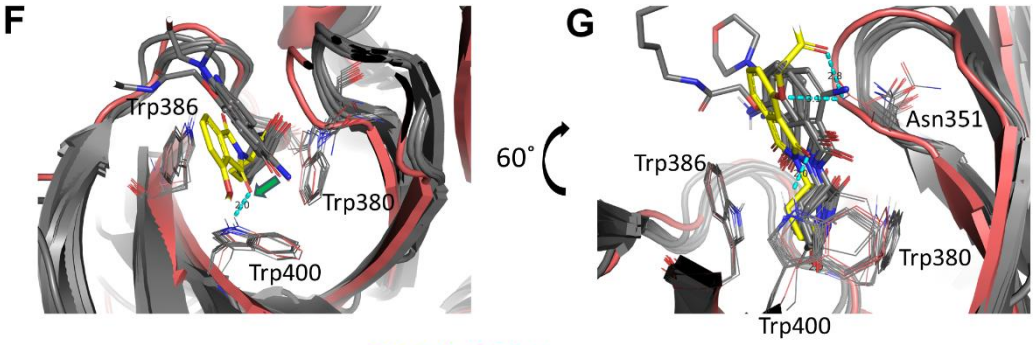


Figure 2. PS-2/PS-10 degrades BTK through a molecular glue mechanism.

A. Experiment scheme for binary binding TR-FRET assay. Degrader, with or without CRBN, will compete with a fluorescent BTK tracer for BTK pocket binding. Successful displacement of the tracer from the BTK pocket by the degrader results in a reduction of TR-FRET signal. **B**. BTK full length TR-FRET binary binding

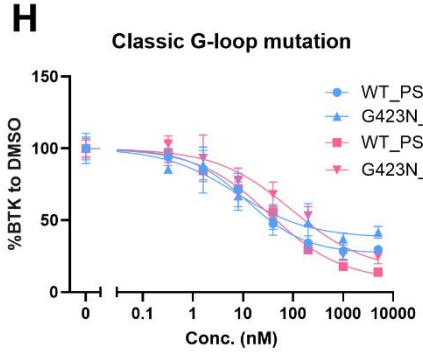
experiment with 1h PS-2 or PS-10 treatment with or without CRBN (1/5 molarity of the compound). CRBN-PS binary complex concentrations are calculated from one-site binding equilibrium equation using K_d values between CRBN and compound (see methods for detail). TR-FRET ratios were normalized to DMSO-treated samples. **C**. TR-FRET binary binding experiment with 1h PS-2, PS-10, PS-10-Me, or pomalidomide treatment with or without BTK (equal molarity to the compound). TR-FRET ratios were normalized to DMSO-treated samples. **D.** Experiment scheme for ternary binding TR-FRET assay. Degrader brings Tb antibody-labeled BTK and fluorescence-labeled His-CRBN/DDB1 into proximity and results in TR-FRET signal increase. **E.** TR-FRET ternary binding experiment using MBP-BTK full length with 1h PS-2, PS-10 and PS-10-Me with or without 5 μM ibrutinib competition. **F.G.** Immunoblots of PS-2- or PS-10-induced BTK degradation in the absence or presence of PS-W competition in Ramos cell for 24h treatment.

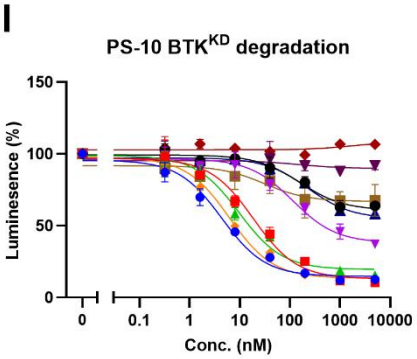




PS-10 CRBN (this work)

CRBN-ligands from PDB

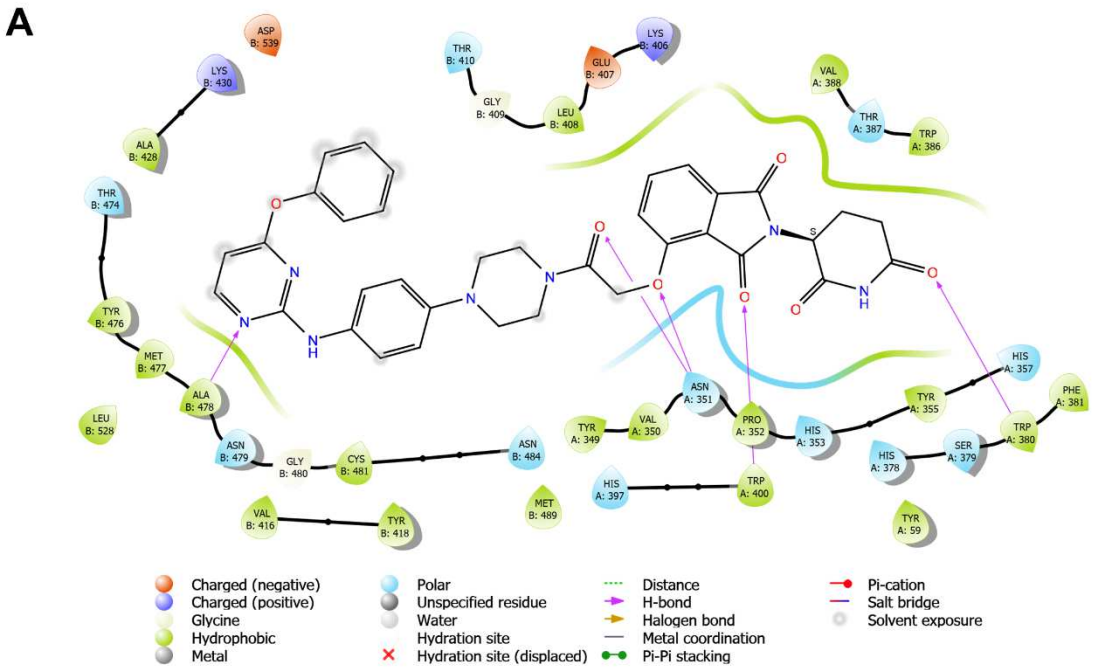


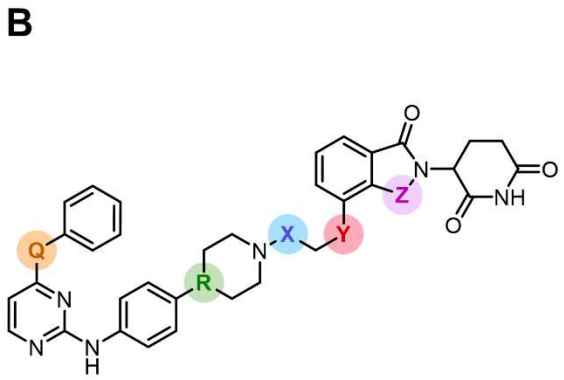


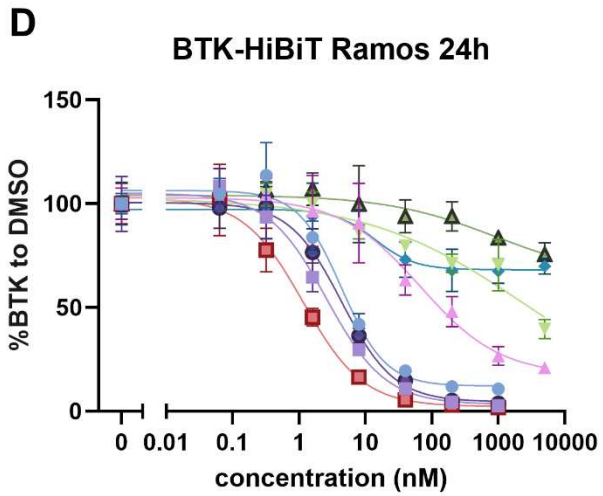
	DC_{50}	D_{max}
WT	6.2 nM	85%
K406A	26.0 nM	87%
E407A	18.3 nM	81%
K420A	638 nM	62%
E488A	8.8 nM	87%
K420A/E488A	-	39%
K406A/K420A	-	33%
E407A/K420A	-	45%
K406A/E407A/K420A	-	10%
K406A/E407A/K420A/E488A	-	-

Figure 3. Cryo-EM structure of CRBN-PS-10-BTK ternary complex.

A. Cryo-EM structure model of CRBN-PS-10-BTK complex (Resolution 3.42 Å). Colored frames are zoomed-in in corresponding panel C, D, and E. **B**. PS-10 electron density (yellow mesh) and its hydrogen bond interaction (cyan dashes) with BTK (blue) and CRBN (pink). **C.D.E**. Zoomed-in protein-protein interface as highlighted in panel A between CRBN and BTK kinase domain with hydrogen bonds (yellow dashes). **F.G**. CRBN tri-tryptophan pocket (pink from this study 9YTE, grey from 5FQD, 6BN7, 6H0F, 6UML, 8D81, 8TNQ, 8U16) with bound ligands (grey, with heteroatom colored) or PS-10 (yellow). Tryptophan residues 380, 386, 400 were aligned. Hydrogen bonds are highlighted in cyan. The translation of pomalidomide is highlighted with a green arrow. **H**. PS-2 or PS-10 induced BTK full length-HiBiT degradation with or without G423N mutation in the classic G-loop in HeLa cell for 24h treatment. **I**. BTK kinase domain-HiBiT degradation assay with various PPI point mutations on kinase domain, in HeLa cell treated with serial dilution of PS-10 for 24h. Shown are mean ± SD luminescence values normalized to DMSO-treated samples.







C

Compound	Q	R	X	Y	Z
PS-2	O	N	C=O	NH	C=O
PS-10	O	N	C=O	O	C=O
PS-13	O	N	CH_2	NH	C=O
PS-16	O	N	C=O	NH	CH_2
PS-22	O	N	C=O	O	CH_2
PS-29	NH	N	C=O	NH	C=O
PS-31	NH	N	C=O	O	C=O
PS-32	O	CH	C=O	NH	C=O

	DC_{50} (nM)	D_{max} (%)
PS-2	6.0	88
PS-10	3.1	97
PS-13	131.2	83
PS-16	2852	ND
PS-22	-	33
PS-29	4.9	95
PS-31	1.3	98
PS-32	ND	ND

Figure 4. Structure-activity relationship of PS-10-based molecular glues.

A. Ligand interaction diagram of PS-10 within BTK and CRBN pockets. **B.C.** Compounds tested in the BTK degradation assay in panel D. High saturation colors in the table indicate the compounds sharing the same functional groups as PS-10**. D**. BTK-HiBiT degradation assay in Ramos BTK-HiBiT knock-in cell line treated with serial dilution of compounds for 24h. Shown are mean ± SD luminescence values normalized to DMSO-treated samples.

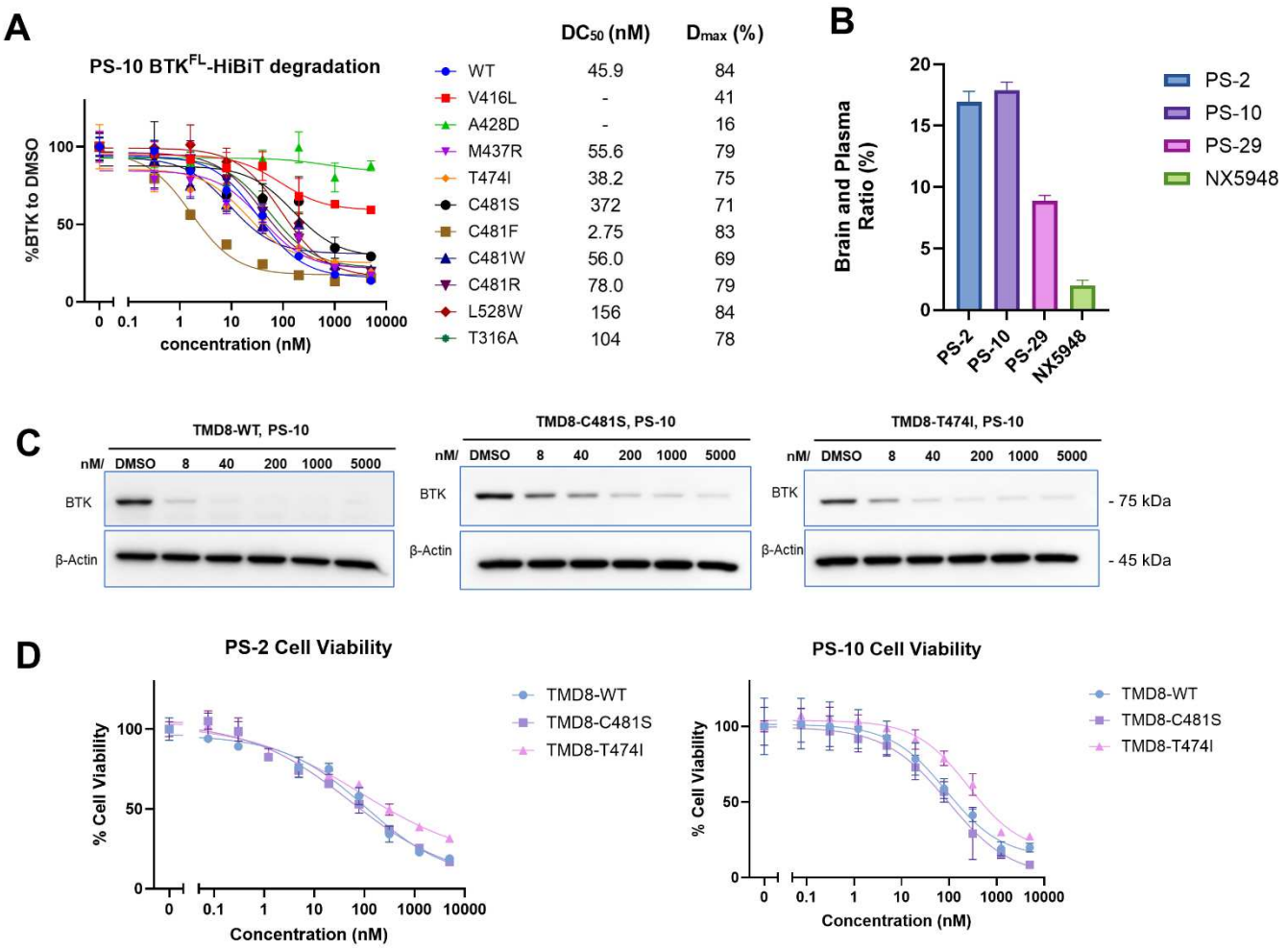


Figure 5. Advantage of PS-10 as a molecular glue.

A. BTK full length-HiBiT degradation assay with various clinical point mutations, in HeLa cell treated with serial dilution of PS-10 for 24h. Shown are mean ± SD luminescence values normalized to DMSO-treated samples. **B.** Brain and Plasma concentration ratio of PS-2, PS-10, PS-29 and NX5948 for 2.17 μmol/kg IV Dose in 5 min. **C.** Immunoblots of PS-10-induced BTK degradation in TMD8-WT, TMD8-C481S and TMD8-T474I cells for 24h treatment. **D**. Cell toxicity of PS-2 and PS-10 in TMD8-WT, TMD8-C481S and TMD8-T474I cells for 72h treatment. Shown are mean ± SD luminescence values normalized to DMSO-treat.

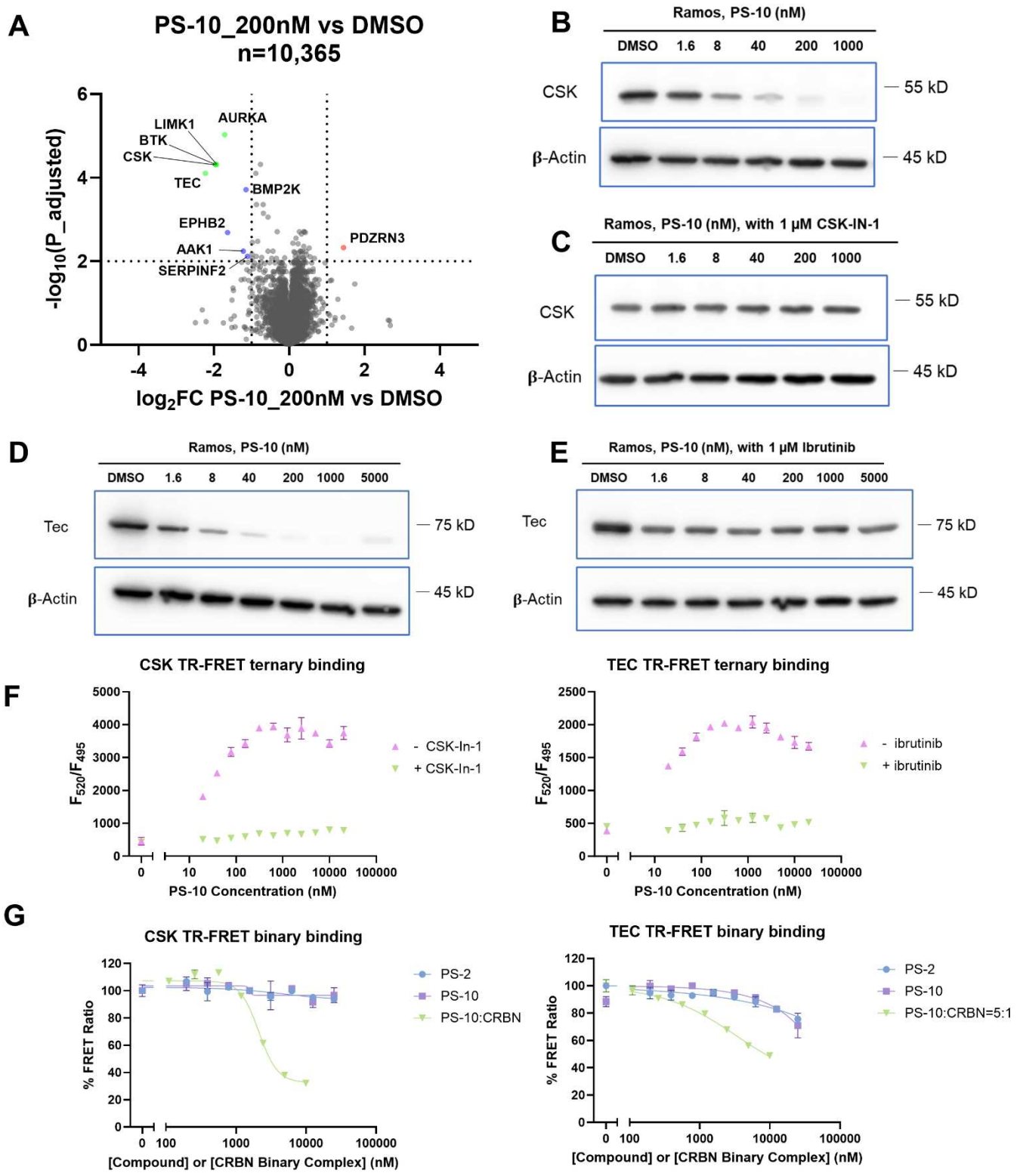


Figure 6. Identify other kinases can be degraded by PS-10 with same mechanism.

A Proteomic analysis showing PS-10 could also degrade CSK, LIMK1, AURKA and TEC other than BTK. Ramos cells were treated with 200nM compounds or DMSO for 24 h. **B-E.** Immunoblots of PS-10-induced CSK and TEC degradation in the absence or presence of competition in Ramos cell for 24h treatment. **F-G.** TR-FRET ternary binding experiment for CSK or TEC and PS-10 with or without inhibitor competition. **G**. TR-

FRET binary binding experiment of CSK or TEC with PS-10 treatment with or without CRBN (1/5 molarity of the compound). CRBN-PS-10 binary complex concentrations are calculated from one-site binding equilibrium equation using K_d values between CRBN and compound (see methods for detail). TR-FRET ratio was normalized to DMSO-treated samples.

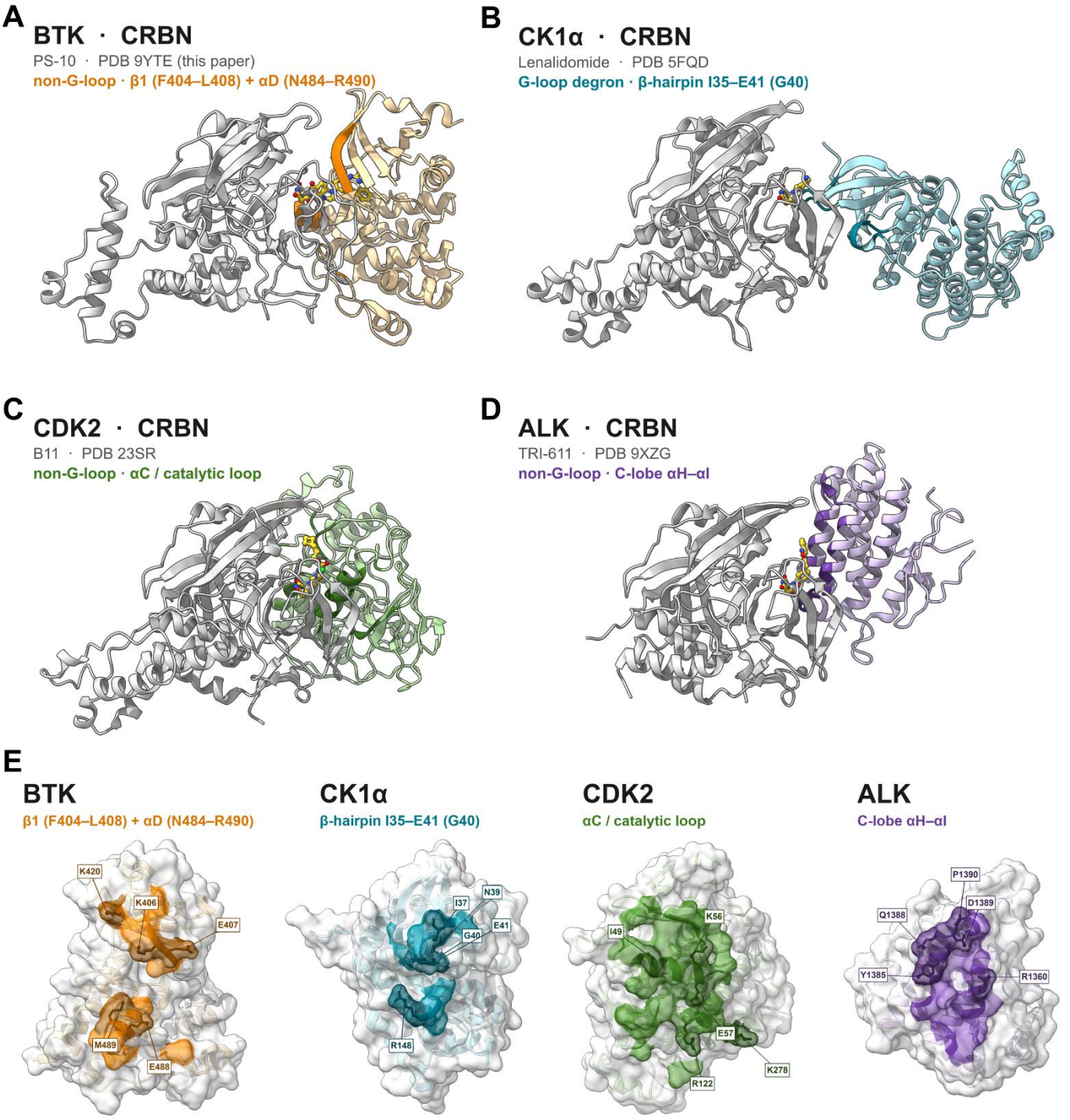


Figure 7. Four structurally distinct kinase surfaces support CRBN molecular glue recognition.

A–D. Ternary complexes of CRBN (grey) with (A) BTK and PS-10 (this study, PDB 9YTE), (B) CK1α and lenalidomide (PDB 5FQD), (C) CDK2 and B11 (PDB 23SR), and (D) ALK and TRI-611 (PDB 9XZG). All four complexes were superposed on the CRBN thalidomide-binding domain (residues 318–425) and are displayed in the same orientation and at the same scale; DDB1 omitted for clarity. Each kinase is shown in a pale tone with its CRBN-contacting residues (any heavy atom within 4.5 Å of CRBN) in the corresponding

saturated tone; glues are drawn as yellow ball-and-stick with heteroatoms colored, **E.** The same CRBN-contacting surfaces mapped onto the isolated kinase domains.

Supplementary Figures

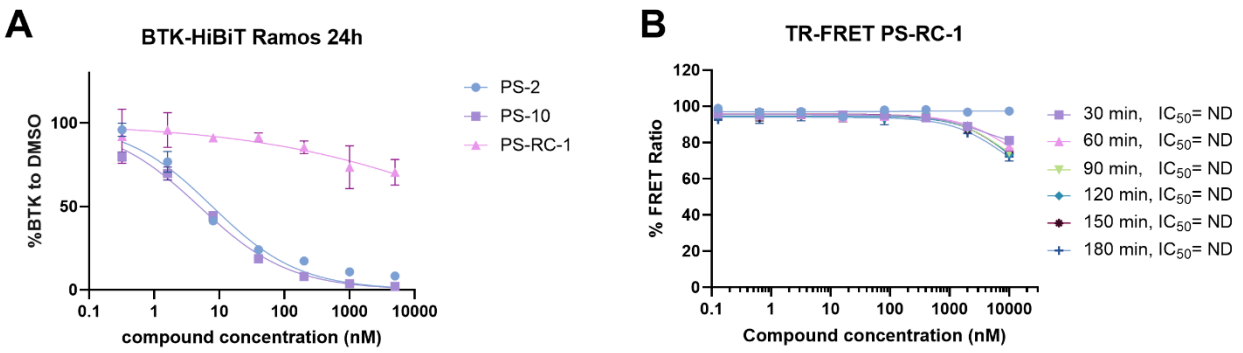


Figure S1. PS-RC-1 is a less potent BTK degrader compared with PS-2 or PS-10 (A) and exhibits weak binding affinity towards BTK in the binary TR-FRET assay (B).

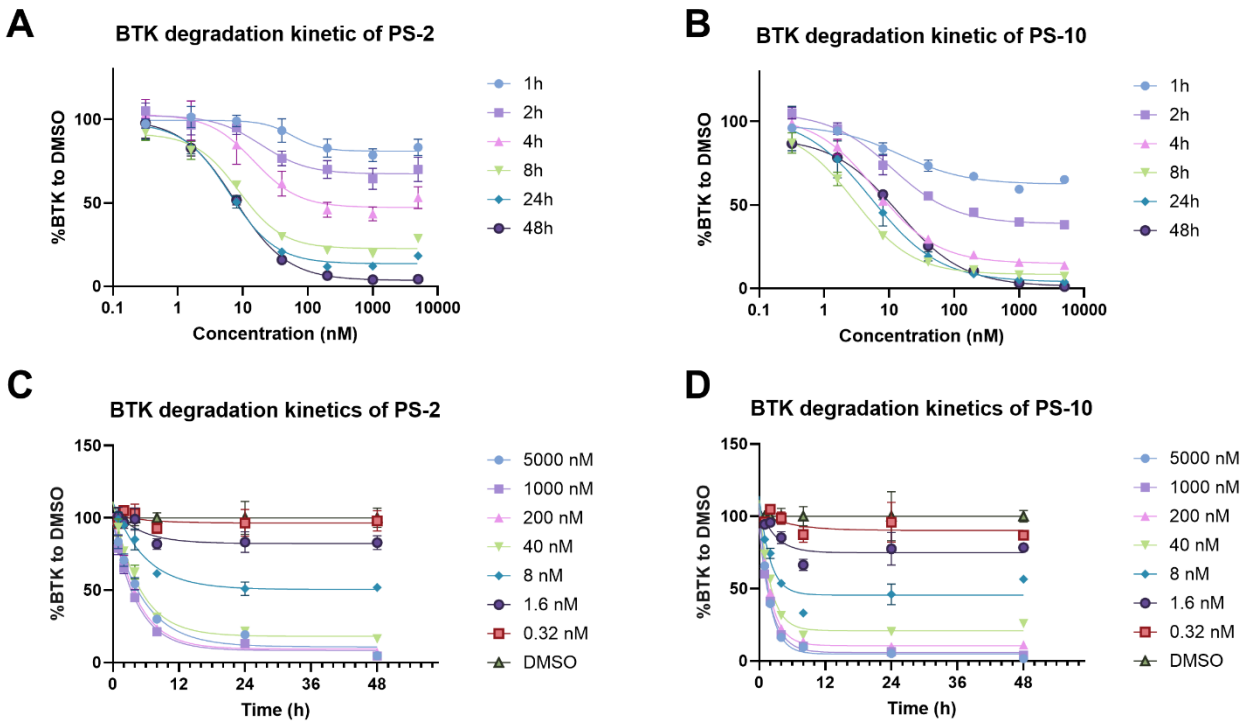


Figure S2. BTK degradation kinetics by PS-2 (A,C) and PS-10 (B,D) in Ramos BTK-HiBiT knock-in cell line.

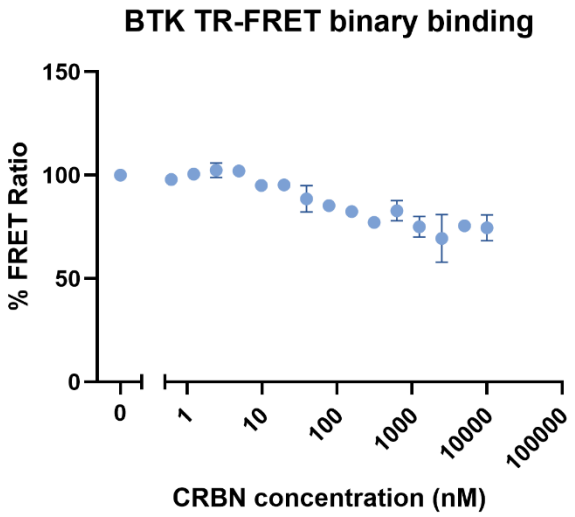


Figure S3. Binary TR-FRET on the BTK side without any compound shows BTK has weak basal binding affinity with CRBN.

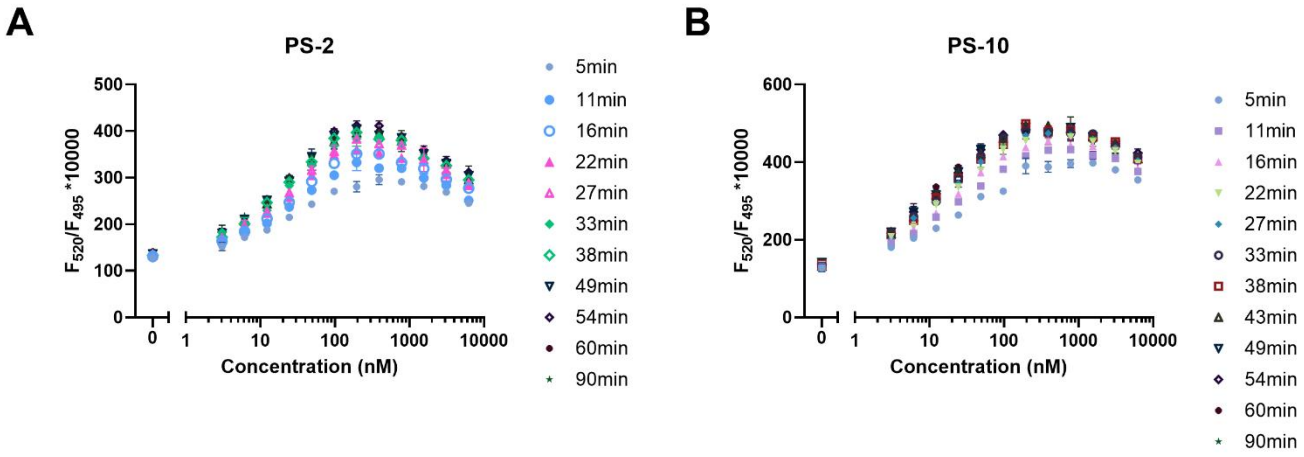


Figure S4. Ternary complex formation kinetics of PS-2 (A), PS-10 (B) by ternary TR-FRET.

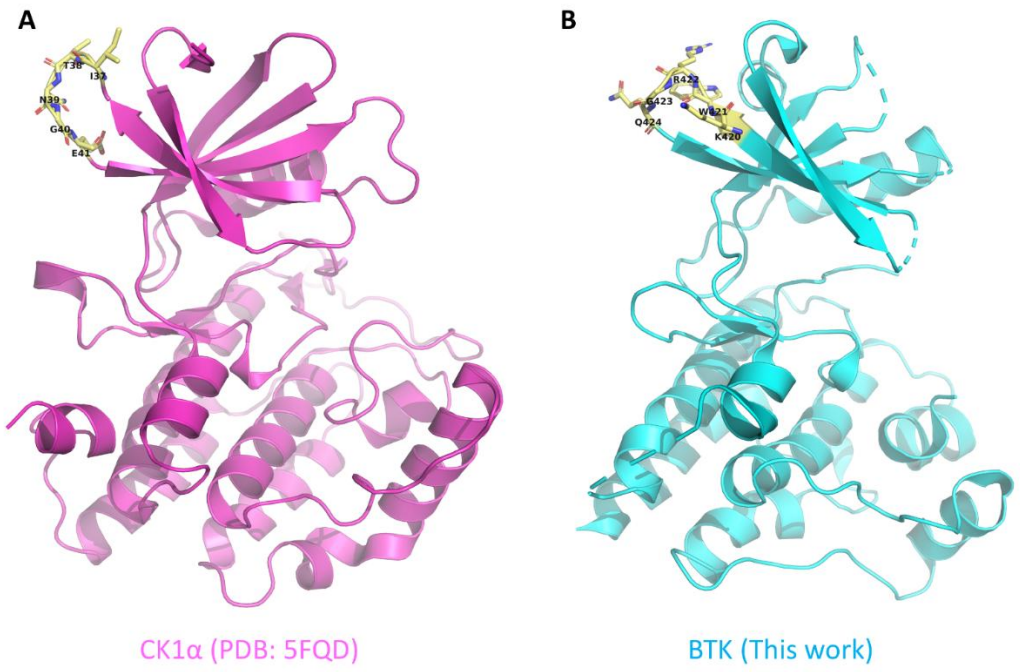


Figure S5. Comparison of CK1α G loop residue 37-41 (A) and BTK "putative G loop" residue 420-424 (B) in yellow shows different backbone shape and carbonyl direction.

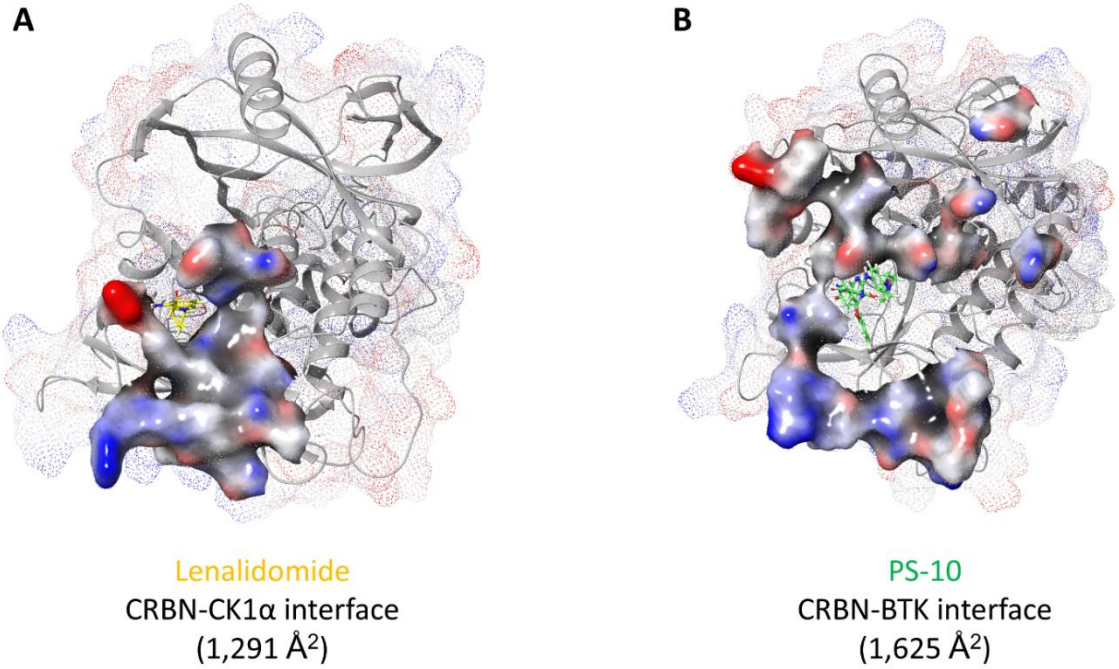


Figure S6. Comparison of buried surfaces and their areas on CRBN-target protein complex between lenalidomide-induced CK1α G-loop interface (A) and PS-10 induced BTK kinase domain interface (B).

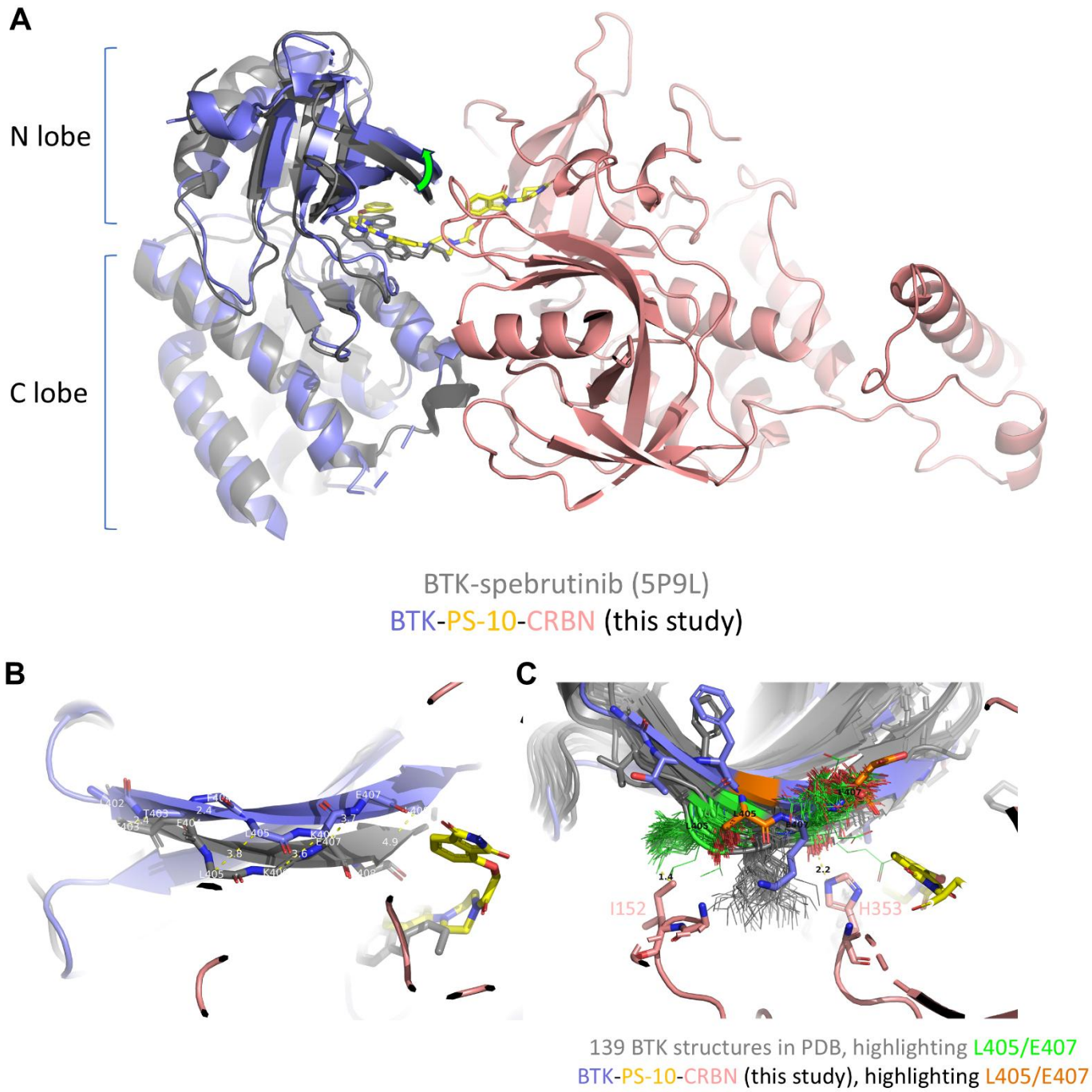


Figure S7. BTK N-lobe is twisted to accommodate for the CRBN-PS-10 ternary complex formation.

(A) Structure comparison between BTK-PS-10-CRBN complex and BTK-spebrutinib crystal structure (grey, PDB: 5P9L) demonstrates the kinase domain N lobe undergo a small angle rotation (green arrow). **(B)** Zoom-in view of panel A focusing on the β1 strand of BTK kinase domain. Yellow dotted lines shown are the Cα atom distances between the two structures. **(C)** Alignment of 139 available BTK kinase structures in PDB with PS-10-induced BTK structure. L405 and E407 are colored in green (PDB structures) and orange (PS-10-induced structure).

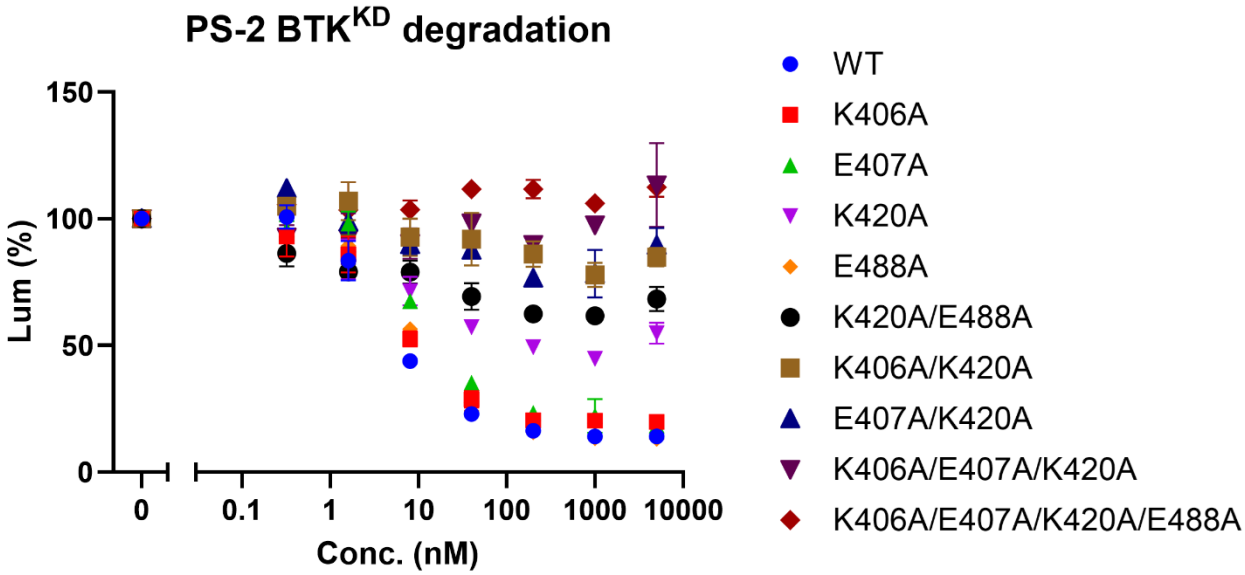


Figure S8. BTK kinase domain-HiBiT degradation assay with various PPI point mutations on the kinase domain, in HeLa cell treated with serial dilution of PS-2 for 24 hours. Shown are mean ± SD luminescence values normalized to DMSO-treated samples.

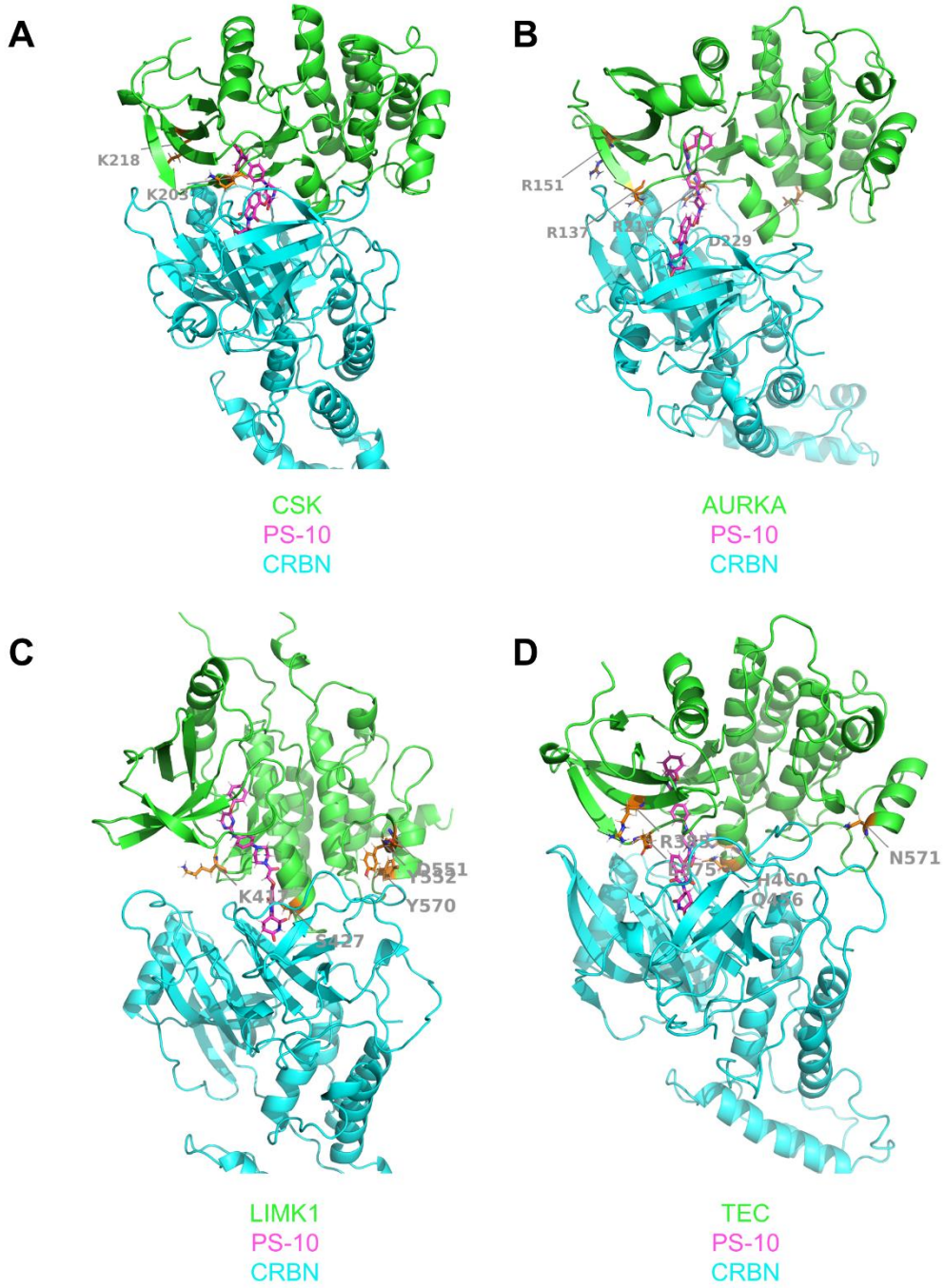
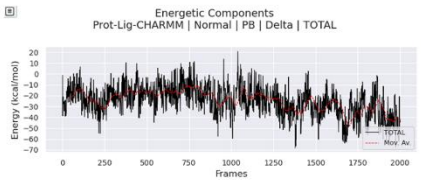
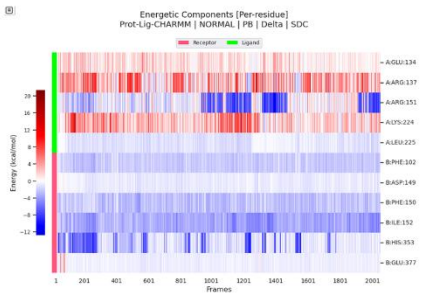


Figure S9. The last frame of MD simulations (200 ns) whose starting conformations were modeled by aligning different kinase domains to the BTK part in the BTK-PS-10-CRBN cryo-EM structure. A. CSK; B. AURKA; C. LIMK1; D. TEC.

HB analysis using in-house scripts

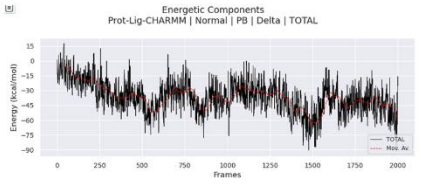
AURKA

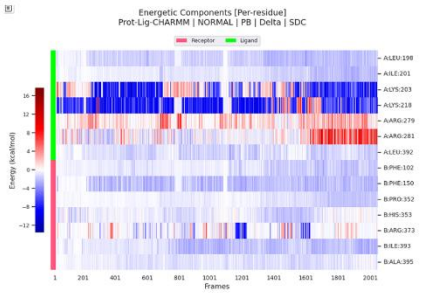


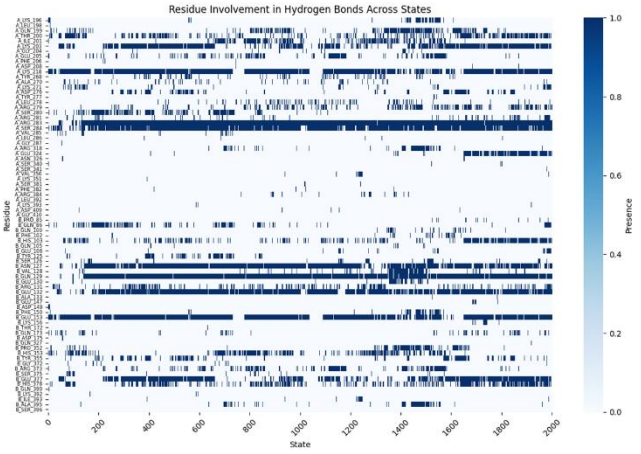




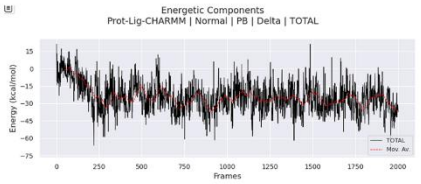
CSK

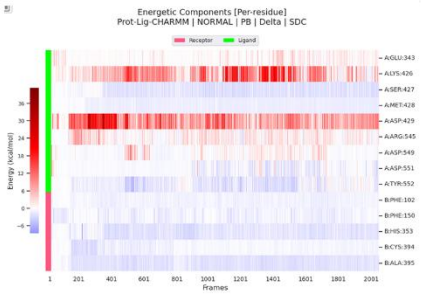


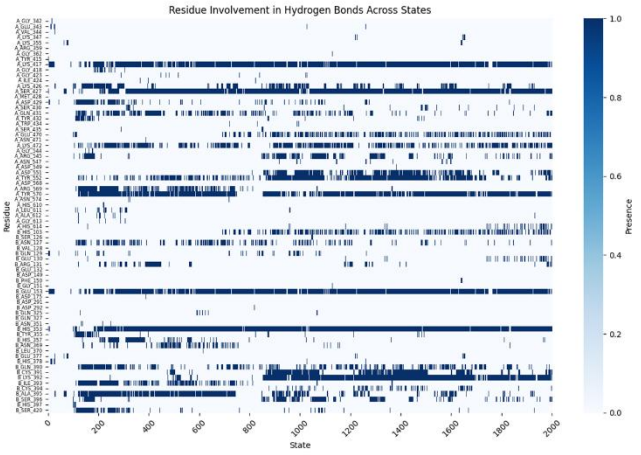




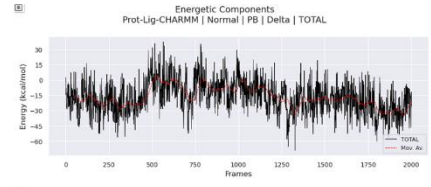
LIMK1

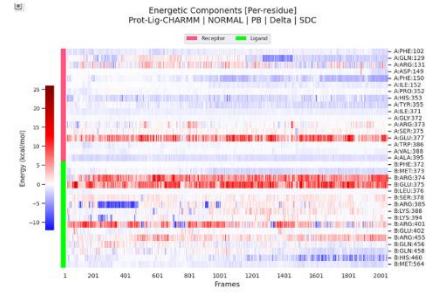






TEC





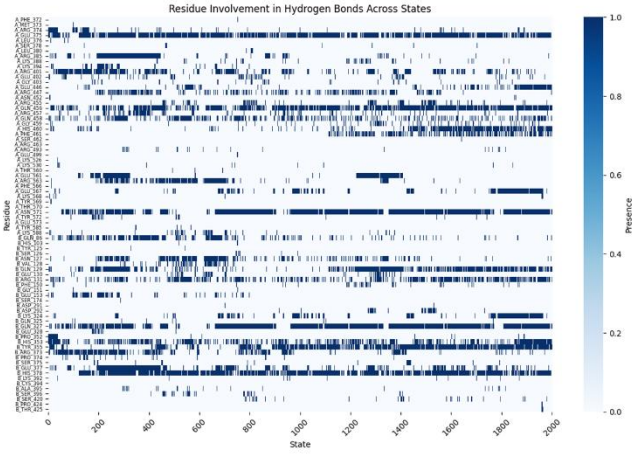


Figure S10. MM-PBSA analysis (each kinase upper left: total energy; bottom left: residual side chain decomposition energy) and hydrogen bond analysis (right) of the MD simulation trajectories whose starting conformations were modeled by aligning different kinase domains to the BTK part in the BTK-PS-10-CRBN cryo-EM structure. In the residual side chain energy decomposition panels, receptor is defined as CRBN, and ligand is defined as kinase domains.

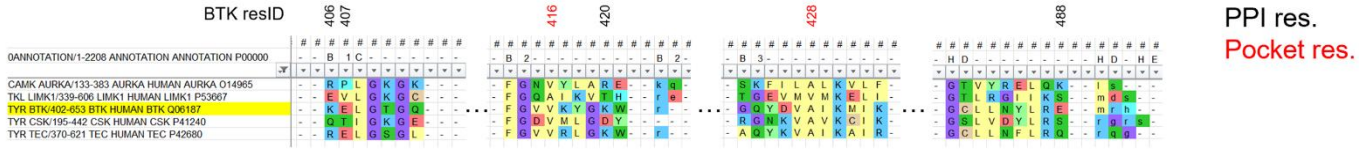


Figure S11. Sequence alignment of BTK and other PS-10 off-target proteins, highlighting the residues involved in the CRBN-BTK PPI (black) and BTK kinase pocket (red).

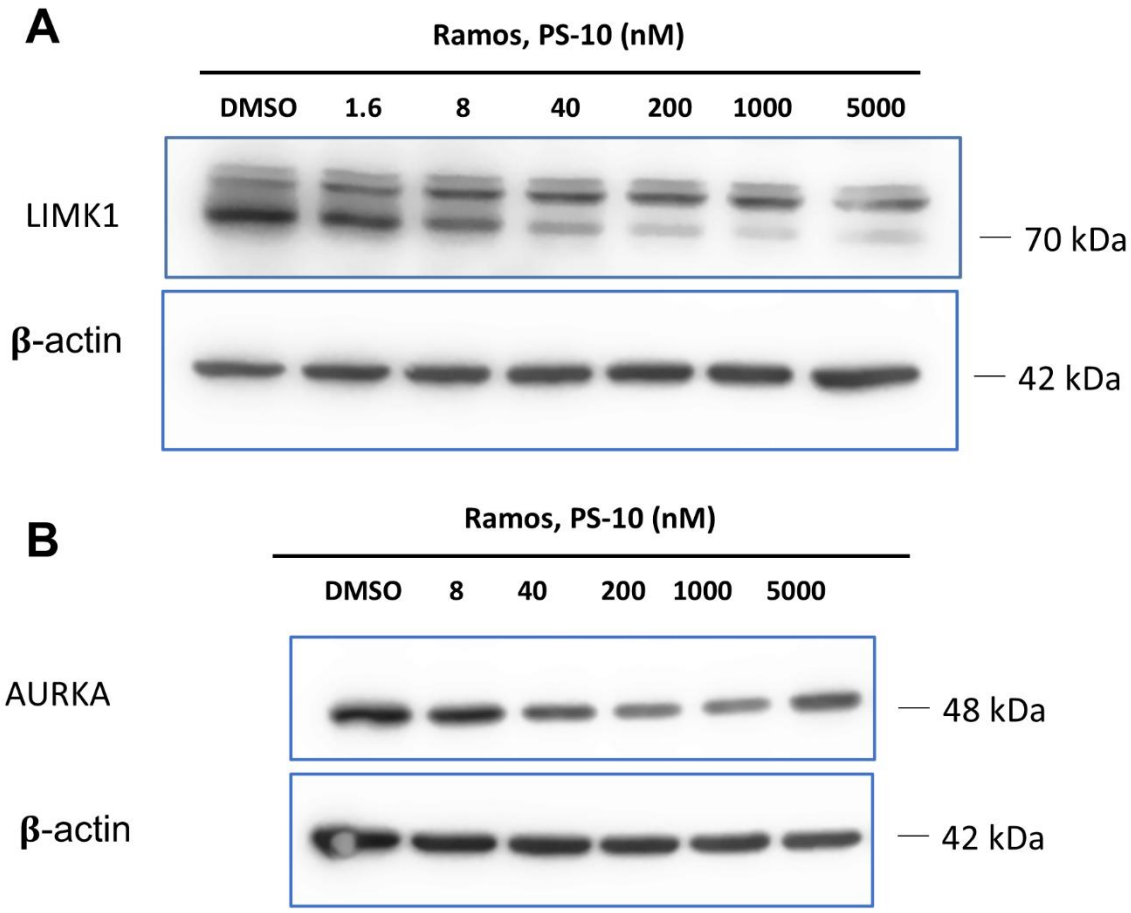


Figure S12. Immunoblots of PS-10-induced LIMK1 and AURKA degradation in Ramos cell for 24h PS-10 treatment.

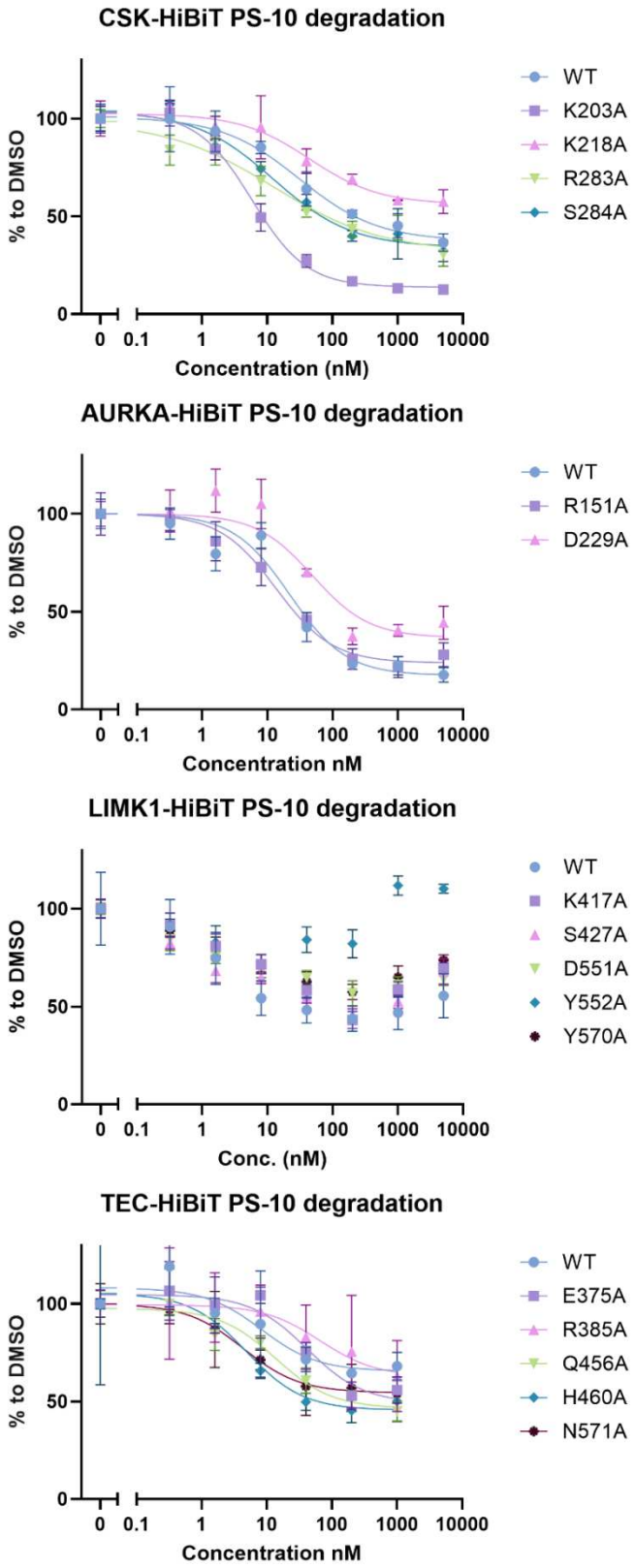


Figure S13. Kinase domain-HiBiT degradation assay with transient transfection of various mutants in HeLa cell, treated with serial dilution of PS-10 for 24h. Shown are mean ± SD luminescence values normalized to DMSO-treated samples (n=3).

References

1. Krönke J, Udeshi ND, Narla A, Grauman P, Hurst SN, McConkey M, et al. Lenalidomide Causes Selective Degradation of IKZF1 and IKZF3 in Multiple Myeloma Cells. Science. 2014 Jan 17;343(6168):301–5. doi:10.1126/science.1244851

2. Fischer ES, Böhm K, Lydeard JR, Yang H, Stadler MB, Cavadini S, et al. Structure of the DDB1–CRBN E3 ubiquitin ligase in complex with thalidomide. Nature. 2014 Aug;512(7512):49–53. doi:10.1038/nature13527

3. Petzold G, Fischer ES, Thomä NH. Structural basis of lenalidomide-induced CK1α degradation by the CRL4(CRBN) ubiquitin ligase. Nature. 2016 Apr 7;532(7597):127–30. doi:10.1038/nature16979 PubMed PMID: 26909574.

4. Matyskiela ME, Lu G, Ito T, Pagarigan B, Lu CC, Miller K, et al. A novel cereblon modulator recruits GSPT1 to the CRL4CRBN ubiquitin ligase. Nature. 2016 Jul;535(7611):252–7. doi:10.1038/nature18611

5. Sievers QL, Petzold G, Bunker RD, Renneville A, Słabicki M, Liddicoat BJ, et al. Defining the human C2H2 zinc finger degrome targeted by thalidomide analogs through CRBN. Science. 2018 Nov 2;362(6414):eaat0572. doi:10.1126/science.aat0572

6. Oleinikovas V, Gainza P, Ryckmans T, Fasching B, Thomä NH. From thalidomide to rational molecular glue design for targeted protein degradation. Annu Rev Pharmacol Toxicol. 2024 Jan 23;64(1):291–312. Located at: www.annualreviews.org. doi:10.1146/annurev-pharmtox-022123-104147 PubMed PMID: 37585660.

7. Hanzl A, Inghelram C, Schmitt S, Thomä NH. Primed for degradation: How weak protein interactions enable molecular glue degraders. Curr Opin Struct Biol. 2025 Jun 1;92:103052. doi:10.1016/j.sbi.2025.103052

8. Kozicka Z. Clues for glues: from serendipity to nature's blueprints in degrader discovery. Essays Biochem. 2025 Dec 22;69(04):379–91. doi:10.1042/EBC20253058

9. Schreiber SL. The Rise of Molecular Glues. Cell. 2021 Jan;184(1):3–9. doi:10.1016/j.cell.2020.12.020

10. Cao S, Kang S, Mao H, Yao J, Gu L, Zheng N. Defining molecular glues with a dual-nanobody cannabidiol sensor. Nat Commun. 2022 Feb 10;13(1):815. doi:10.1038/s41467-022-28507-1 PubMed PMID: 35145136; PubMed Central PMCID: PMC8831599.

11. Petzold G, Gainza P, Annunziato S, Lamberto I, Trenh P, McAllister LA, et al. Mining the CRBN target space redefines rules for molecular glue–induced neosubstrate recognition. Science. 2025 Jul 3;389(6755):eadt6736. doi:10.1126/science.adt6736

12. Monte Rosa Therapeutics, Inc. Phase 1, First-in-Human, Randomized, Double-Blind, Placebo-Controlled, Single Ascending Dose, Multiple Ascending Dose, and Food-Effect Study to Assess Safety, Tolerability, PK and PD of MRT-6160 in Healthy Subjects [Clinical trial registration] [Internet]. clinicaltrials.gov; 2025 Jul [cited 2026 May 19]. Clinical trial registration no.: NCT06597799. Available from: https://clinicaltrials.gov/study/NCT06597799

13. Cartwright ANR. MRT-6160, a highly selective and first-in-class VAV1-directed molecular glue degrader, demonstrates activity in multiple immune-mediated disease models. Keystone

Symposia - Autoimmunity & Autoinflammation: Translating Basic Mechanisms into Novel Therapeutic Approaches (A2). 2026 Jan 21; Keystone, CO, USA.

14. Lin H, Yu X, Zheng H, Cheng R, Zhang M, Qi X, et al. Leveraging high-throughput proteomics and AI-based protein folding to accelerate VAV1 molecular glue discovery. Nat Commun. 2026 Sep 12. doi:10.1038/s41467-026-77657-z

15. Lin H, Yang YY, Maity S, Sun Q, Wang J. Ultrahigh-Throughput Liquid Chromatography with Tandem Mass Spectrometry Method for Targeted Protein Degradation Compound Screening Using the Orbitrap Astral Mass Spectrometer. J Proteome Res. 2026 May 5;acs.jproteome.5c01023. doi:10.1021/acs.jproteome.5c01023

16. Annunziato S, Quan C, Donckele EJ, Lamberto I, Bunker RD, Zlotosch M, et al. Cereblon induces G3BP2 neosubstrate degradation using molecular surface mimicry. Nat Struct Mol Biol. 2026 Mar;33(3):479–87. doi:10.1038/s41594-025-01738-8

17. Langousis G, Gainza P, Hunkeler M, Kapsitidou D, Donckele EJ, Annunziato S, et al. A degron-mimicking molecular glue drives CRBN homo-dimerization and degradation. Nat Commun. 2025 Nov 19;16(1):10157. doi:10.1038/s41467-025-65094-3

18. Shrivastav P, Singh R, Wiemer AJ. Molecular glues evolve from serendipity to rational design. Trends Pharmacol Sci. 2026 Jan;47(1):85–99. doi:10.1016/j.tips.2025.10.013

19. Vetrie D, Vořechovský I, Sideras P, Holland J, Davies A, Flinter F, et al. The gene involved in X-linked agammaglobulinaemia is a member of the src family of protein-tyrosine kinases. Nature. 1993 Jan 21;361(6409):226–33. doi:10.1038/361226a0

20. Tsukada S, Saffran DC, Rawlings DJ, Parolini O, Allen RC, Klisak I, et al. Deficient expression of a B cell cytoplasmic tyrosine kinase in human X-linked agammaglobulinemia. Cell. 1993 Jan;72(2):279–90. doi:10.1016/0092-8674(93)90667-F

21. Byrd JC, Furman RR, Coutre SE, Flinn IW, Burger JA, Blum KA, et al. Targeting BTK with Ibrutinib in Relapsed Chronic Lymphocytic Leukemia. N Engl J Med. 2013 Jul 4;369(1):32–42. doi:10.1056/NEJMoa1215637

22. Woyach JA, Furman RR, Liu TM, Ozer HG, Zapatka M, Ruppert AS, et al. Resistance Mechanisms for the Bruton's Tyrosine Kinase Inhibitor Ibrutinib. N Engl J Med. 2014 Jun 12;370(24):2286–94. doi:10.1056/NEJMoa1400029

23. Wang E, Mi X, Thompson MC, Montoya S, Notti RQ, Afaghani J, et al. Mechanisms of Resistance to Noncovalent Bruton's Tyrosine Kinase Inhibitors. N Engl J Med. 2022 Feb 24;386(8):735–43. doi:10.1056/NEJMoa2114110

24. Mato AR, Woyach JA, Brown JR, Ghia P, Patel K, Eyre TA, et al. Pirtobrutinib after a Covalent BTK Inhibitor in Chronic Lymphocytic Leukemia. N Engl J Med. 2023 Jul 6;389(1):33–44. doi:10.1056/NEJMoa2300696

25. Shah N, Huntington S, Lewis D, Munir T, Collins G, Alencar A, et al. Bexobrutideg (NX-5948), a novel Bruton's tyrosine kinase (BTK) degrader, shows high clinical activity and tolerable safety in patients with Waldenström macroglobulinemia: Updated results from an ongoing Phase 1a/b study. Blood. 2025 Nov 3;146(Supplement 1):5359–5359. doi:10.1182/blood-2025-5359

26. Seymour JF, Tam CS, Cheah CY, Parrondo RD, Allan JN, Trotman J, et al. Preliminary Efficacy and Safety of the Bruton Tyrosine Kinase Degrader BGB-16673 in Patients with Relapsed or Refractory

Waldenström Macroglobulinemia: Results from the Phase 1 CaDAnCe-101 Study. Blood. 2024 Nov 5;144(Supplement 1):860–860. doi:10.1182/blood-2024-199212

27. Li N, Sheng J, Zhu HH. Breakthroughs in treatment for hematological malignancies: latest updates on molecular glue, PROTACs and RNA degraders from ASH 2024. J Hematol OncolJ Hematol Oncol. 2025 Mar 5;18(1):26. doi:10.1186/s13045-025-01674-6

28. Guo WH, Qi X, Yu X, Liu Y, Chung CI, Bai F, et al. Enhancing intracellular accumulation and target engagement of PROTACs with reversible covalent chemistry. Nat Commun. 2020 Aug 26;11(1):4268. doi:10.1038/s41467-020-17997-6 PubMed PMID: 32848159; PubMed Central PMCID: PMC7450057.

29. Park JK, Byun JY, Park JA, Kim YY, Lee YJ, Oh JI, et al. HM71224, a novel Bruton's tyrosine kinase inhibitor, suppresses B cell and monocyte activation and ameliorates arthritis in a mouse model: a potential drug for rheumatoid arthritis. Arthritis Res Ther. 2016 Dec;18(1):91. doi:10.1186/s13075-016-0988-z

30. Yu X, Guo WH, Lin H, Cheng R, Monroy EY, Jin F, et al. Discovery of a potent BTK and IKZF1/3 triple degrader through reversible covalent BTK PROTAC development. Curr Res Chem Biol. 2022;2:100029. doi:10.1016/j.crchbi.2022.100029 PubMed PMID: 36712232; PubMed Central PMCID: PMC9879287.

31. Cruite JT, Nowak RP, Donovan KA, Ficarro SB, Huang H, Liu H, et al. Covalent Stapling of the Cereblon Sensor Loop Histidine Using Sulfur-Heterocycle Exchange. ACS Med Chem Lett. 2023 Oct 24;acsmedchemlett.3c00371. doi:10.1021/acsmedchemlett.3c00371

32. Watson ER, Novick S, Matyskiela ME, Chamberlain PP, H de la Peña A, Zhu J, et al. Molecular glue CELMoD compounds are regulators of cereblon conformation. Science. 2022 Nov 4;378(6619):549–53. doi:10.1126/science.add7574 PubMed PMID: 36378961; PubMed Central PMCID: PMC9714526.

33. Cheng S, Guo A, Lu P, Ma J, Coleman M, Wang YL. Functional characterization of BTK(C481S) mutation that confers ibrutinib resistance: exploration of alternative kinase inhibitors. Leukemia. 2015 Apr;29(4):895–900. doi:10.1038/leu.2014.263

34. Gainza P, Wehrle S, Van Hall-Beauvais A, Marchand A, Scheck A, Harteveld Z, et al. De novo design of protein interactions with learned surface fingerprints. Nature. 2023 May;617(7959):176–84. doi:10.1038/s41586-023-05993-x

35. Pei Y, Lin W, Li X, Meng Y, Yin Y, Pan B, et al. Selective CDK2 Degradation via Noncanonical Recruitment. J Med Chem. 2026 Jul 9;69(13):15996–6024. doi:10.1021/acs.jmedchem.6c01264 PubMed PMID: 42334090.

36. Conery AR, La DS, Alekseyenko AA, Marcoux D, Bart AG, Harlow ML, et al. TRI-611, a selective, brain-penetrant molecular glue degrader of ALK. Nature. 2026 Sep 9;1–9. doi:10.1038/s41586-026-10998-3

37. Sievers Q, Lu H, Cool A, Gajewski S, Kong T, Noviski MA, et al. Molecular and Structural Basis of Pan-Resistance to BTK Degraders and Inhibitors. Cancer Discov. 2026 Jul 22. doi:10.1158/2159-8290.CD-26-0251

38. Wei J, Feng W, Chen Q, Li Q, Chen Z. Rational discovery of molecular glue degraders based on block chemistry. Drug Discov Today. 2025 Nov 1;30(11):104480. doi:10.1016/j.drudis.2025.104480

39. Lin H, Riching K, Lai MP, Lu D, Cheng R, Qi X, et al. Lysineless HiBiT and NanoLuc Tagging Systems as Alternative Tools for Monitoring Targeted Protein Degradation. ACS Med Chem Lett. 2024 Aug 8;15(8):1367–75. doi:10.1021/acsmedchemlett.4c00271 PubMed PMID: 39140070; PubMed Central PMCID: PMC11318018.

40. Bender AT, Gardberg A, Pereira A, Johnson T, Wu Y, Grenningloh R, et al. Ability of Bruton's Tyrosine Kinase Inhibitors to Sequester Y551 and Prevent Phosphorylation Determines Potency for Inhibition of Fc Receptor but not B-Cell Receptor Signaling. Mol Pharmacol. 2017 Mar;91(3):208–19. doi:10.1124/mol.116.107037 PubMed PMID: 28062735.

41. Hughes CS, Foehr S, Garfield DA, Furlong EE, Steinmetz LM, Krijgsveld J. Ultrasensitive proteome analysis using paramagnetic bead technology. Mol Syst Biol. 2014 Oct;10(10):757. doi:10.15252/msb.20145625

42. Hughes CS, Moggridge S, Müller T, Sorensen PH, Morin GB, Krijgsveld J. Single-pot, solid-phase-enhanced sample preparation for proteomics experiments. Nat Protoc. 2019 Jan;14(1):68–85. doi:10.1038/s41596-018-0082-x PubMed PMID: 30464214.

43. Watson ER, Novick S, Matyskiela ME, Chamberlain PP, H. De La Peña A, Zhu J, et al. Molecular glue CELMoD compounds are regulators of cereblon conformation. Science. 2022 Nov 4;378(6619):549–53. doi:10.1126/science.add7574

44. Mastronarde DN. SerialEM: A Program for Automated Tilt Series Acquisition on Tecnai Microscopes Using Prediction of Specimen Position. Microsc Microanal. 2003 Aug 1;9(S02):1182–3. doi:10.1017/S1431927603445911

45. Rohou A, Grigorieff N. CTFFIND4: Fast and accurate defocus estimation from electron micrographs. J Struct Biol. 2015 Nov 1;Recent Advances in Detector Technologies and Applications for Molecular TEM192(2):216–21. doi:10.1016/j.jsb.2015.08.008

46. Scheres SHW. RELION: Implementation of a Bayesian approach to cryo-EM structure determination. J Struct Biol. 2012 Dec 1;180(3):519–30. doi:10.1016/j.jsb.2012.09.006

47. Scheres SHW. A Bayesian View on Cryo-EM Structure Determination. J Mol Biol. 2012 Jan 13;415(2):406–18. doi:10.1016/j.jmb.2011.11.010

48. Kimanius D, Forsberg BO, Scheres SH, Lindahl E. Accelerated cryo-EM structure determination with parallelisation using GPUs in RELION-2. Subramaniam S, editor. eLife. 2016 Nov 15;5:e18722. doi:10.7554/eLife.18722

49. Zivanov J, Nakane T, Forsberg BO, Kimanius D, Hagen WJ, Lindahl E, et al. New tools for automated high-resolution cryo-EM structure determination in RELION-3. Egelman EH, Kuriyan J, editors. eLife. 2018 Nov 9;7:e42166. doi:10.7554/eLife.42166

Supplementary Files

This is a list of supplementary files associated with this preprint. Click to download.

- pdbvalidationoutput.zip
- SI.pdf
- BTKGlueSourceDataandWBgel.xlsx
- CryoEMmapsandmodels.zip